ABSTRACT

Title of Dissertation:	ASSESSING THE THERMAL SAFETY AND THERMOCHEMISTRY OF LITHIUM METAL ALL-SOLID-STATE BATTERIES THROUGH DIFFERENTIAL SCANNING CALORIMETRY AND MODELING
	Nathan Brenner Johnson, Doctor of Philosophy, 2023
Dissertation directed by:	Assistant Professor Paul Albertus Chemical and Biomolecular Engineering

Solid-state batteries are often considered to have superior safety compared to their liquid electrolyte counterparts, but further analysis is needed, especially because the desired higher specific energy of a solid-state lithium metal battery results in a higher potential temperature rise from the electrical energy in the cell. Safety is a multi-faceted issue that should be carefully assessed. We build "all-inclusive microcell" Differential Scanning Calorimetry samples that include all cell stack layers for a $Li_{0.43}CoO2$ | $Li_7La_3Zr_2O_{12}$ | Li cell in commercially relevant material ratios (e.g. capacity matched electrodes) and gather heat flow data. From this data, we use thermodynamically calculated enthalpies of reactions for this cell chemistry to predict key points in cell thermal runaway (e.g., onset temperature, maximum temperature) and assess battery safety at the materials stage of cell development. We construct a model of the temperature rise during a thermal ramp test and short circuit in a large-

format solid-state $Li_{0.43}CoO2$ | $Li_7La_3Zr_2O_{12}$ | Li battery based on microcell heat flow measurements. Our model shows self-heating onset temperatures at ~200-250°C, due to O_2 released from the metal oxide cathode. Cascading exothermic reactions may drive the cell temperature during thermal runaway to ~1000 °C in our model, comparable to temperature rise from high-energy Li-ion cells, but subject to key assumptions such as O_2 reacting with Li. Higher energy density cathode materials such as $LiNi_{0.8}Co_{0.15}Al_{0.05}O_2$ in our model show peak temperatures >1300°C. Transport of O_2 or Li through the solid-state separator (e.g., through cracks), and the passivation of Li metal by solid products such as Li_2O, are key determinants of the peak temperature. Our work demonstrates the critical importance of the management of molten Li and O_2 gas within the cell, and the importance of future modeling and experimental work to quantify the rate of the $2Li+1/2O_2 \rightarrow Li_2O$ reaction, and others, within a large format Li metal solid-state battery.

ASSESSING THE THERMAL SAFETY AND THERMOCHEMISTRY OF LITHIUM METAL ALL-SOLID-STATE BATTERIES THROUGH DIFFERENTIAL SCANNING CALORIMETRY AND MODELING

by

Nathan Brenner Johnson

Dissertation submitted to the Faculty of the Graduate School of the
University of Maryland, College Park, in partial fulfillment
of the requirements for the degree of
Doctor of Philosophy
2023

Advisory Committee:
Assistant Professor Paul Albertus, Chair
Assistant Professor Po-Yen Chen
Associate Professor Yifei Mo
Distinguished Professor Gary Rubloff
Professor Eric Wachsman

Dedication

To my wife, Chelsea, thank you for all your love, encouragement, support, and understanding through these past five years.

To my family, thank you for your encouragement and support.

Acknowledgements

First and foremost, I would like to thank my advisor, Dr. Paul Albertus. His insight and guidance have been invaluable for learning not only electrochemistry, but how to conduct independent research. I could not have asked for a better advisor. I would also like to thank all my current and former fellow lab members over the years: Eric Carmona, Bhuvsmita Bhargava, Mary York, Karl Larson, Dr. Yueming Song, Dr. Caitlin Parke, Dr. Keith Duncan, and Zixuan Wang. Thank you for your patience and help and thank you for all the fun conversations and enjoyable times we've had. Particularly, I'd like to thank Eric whom I spent a lot of time discussing questions and ideas with when we were the only two members of the lab, Bhuvsmita who worked on the same project alongside me. Thank you for always being willing and available for lively, in-depth discussions and for being great friends and colleagues. I'd also like to thank my undergrads, Johnathan Chang, Samaa Zaman, and River Rohrman who have been invaluable for my projects. I'd like to thank our collaborators at Sandia National Lab, Dr. Alex Bates, Dr. Lorraine-Torres-Castro, Dr. Yuliya Preger, and Dr. Randy Shurtz, for their continued discussion and assistance throughout the course of experimental testing. Their help was instrumental in establishing our methods and analysis of our data. I would also like to thank Dr. Aldo Ponce for allowing me access to his facilities and equipment during our experimental testing. I'd like to thank my committee members, Dr. Po-Yen Chen, Dr. Yifei Mo, Dr. Gary Rubloff, and Dr. Eric Wachsman for sitting on my committee and offering their insightful thoughts and questions into this work.

"Research was sponsored by the DEVCOM Army Research Laboratory (ARL) and was funded under Cooperative Agreement (CA) Number W911NF-20-2-0284. The views and conclusions contained in this document are those of the authors and should not be interpreted as representing the official policies, either expressed or implied, of the DEVCOM Army Research Laboratory or the U.S. Government. The U.S. Government is authorized to reproduce and distribute reprints for Government purposes notwithstanding any copyright notation hereon."

Thank you to the A. James and Alice B. Clark foundation for financially supporting me during my doctoral work.

Table of Contents

List of Tables

List of Figures

List of Abbreviations

Lithium metal all-solid-state-battery (LiSSB)

Lithium Lanthanum Zirconium Oxide (LLZO)

Ethylene Carbonate (EC)

Diethyl Carbonate (DEC)

Differential Scanning Calorimetry (DSC)

Finite Element Method (FEM)

Lithium Aluminum Titanium Phosphate (LATP)

Lithium Aluminum Germanium Phosphate (LAGP)

Lithium Lanthanum Titanium Oxide (LLTO)

Ratio of negative to positive electrode capacities (N:P)

Lithium Cobalt Oxide (LCO)

$Li_{6.75}La_3Zr_{1.75}Nb_{0.25}O_{12}$ (LLZNO)

$Li_{6.4}La_3Zr_{1.4}Ta_{0.6}O_{12}$ (LLZTO)

Ordinary Differential Equation (ODE)

Thermogravimetric Analysis (TGA)

State of Charge (SOC)

Poly(vinylidene fluoride) (PVDF)

$LiNi_xMn_yCo_zO_2$ (NMC)

$Li_{10}GeP_2S_{12}$ (LGPS)

$Li_7P_3S_{11}$ (LPS)

$LiNi_{0.8}Co_{0.15}Al_{0.05}O_2$ (NCA)

Chapter 1: Background

As the demand for energy storage increases, the limitations of modern Li-ion cells creates a need for high energy density next-generation batteries.[1] Replacing graphite with lithium metal has a clear potential to increase the specific energy and energy density beyond current state-of-the-art Li-ion batteries due to the high theoretical volumetric and gravimetric energy density of lithium metal compared to modern graphitic anodes.[2,3] Both liquid electrolyte and solid electrolyte approaches to utilizing lithium metal anodes are currently under development, with both facing challenges associated with cycling Li metal under all commercial requirements.[4–7] Solid-electrolytes in particular are thought to offer a mechanically and electrochemically stable lithium interface to suppress dendrite growth and side reactions allowing the safe use of lithium metal anodes.[8,9] In addition to potentially enabling the use of lithium metal anodes, solid electrolytes are also widely perceived as offering superior safety to liquid electrolytes because the carbonate-based liquid electrolytes currently used are unstable at graphite (and Li metal) potentials and lead to self-heating reactions at 80-90°C.[10–12] In addition, at higher temperatures liquid electrolytes can react with O_2 gas, which is released by the cathode upon heating but is also present in the atmosphere into which vaporized electrolyte may be released once a cell vents. The presence of liquid electrolyte within the cathode where O_2 is released limits means to prevent that reaction from occurring. While the thermal safety of Li-ion cells has been widely reported on and modeled, thermal safety of all-

solid-state lithium metal batteries (LiSSB) is still largely unstudied, and the introduction of lithium metal anodes could present new thermal safety problems not seen in modern Li-ion cells. Recently published papers have examined this more closely due to previously unconsidered thermochemical safety concerns in LiSSB such reactivity of lithium metal with oxygen from layered metal oxide and electrolyte decomposition as well as the high reactivity of sulfide ceramics.[13–17] Work by Bates et. al. showed that adiabatic temperature rise following catastrophic separator failure in LiSSB can lead to equivalent thermal runaway temperature rise compared to modern Li-ion in the event of an external heat source, but LiSSB can have 400°C higher temperature rise during short circuits compared to Li-ion.[14] While the onset temperature of LiSSB self-heating is substantially higher than that of modern Li-ion (>170°C compared to 80°C) and the total heat release is generally lower in LiSSB, replacing organic electrolyte with a solid electrolyte will lower the overall heat capacity of the cell resulting in comparable temperature rise.[18–22] Because a principal reason to develop a battery with a solid-state electrolyte is to enable the use of Li metal and increase the cell energy content, it is also important to note that both increasing energy content and replacing a liquid electrolyte with a solid will increase the adiabatic temperature rise from its stored electrical energy, as shown in **Figure 1.1**.

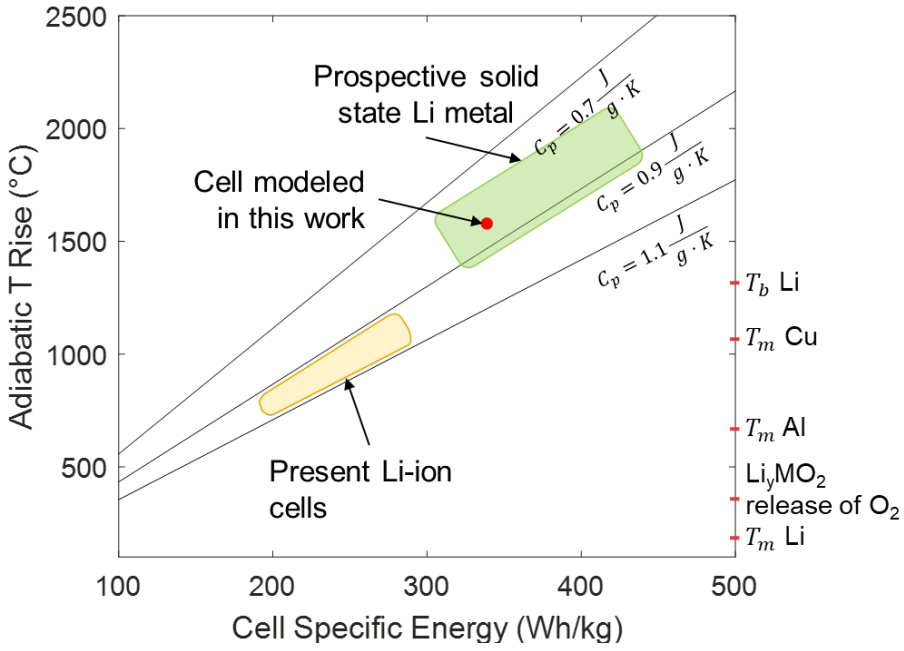

Figure 1.1. The adiabatic temperature rise from stored electrical energy of a cell rises as the cell specific energy increases and the heat capacity falls. T_b indicates a boiling temperature, and T_m indicates a melting temperature. The red point indicates the specific energy of the Li|LLZO|$Li_{0.47}CoO_2$ cell design we model in this work.

In particular, the heat capacity of the common solid electrolyte $Li_7La_3Zr_2O_{12}$ (LLZO) is ~0.68 J/g-K at room temperature, while that of a typical liquid electrolyte (e.g., 1M $LiPF_6$ in EC:DEC) is ~1.8 J/g-K. For cells with comparable properties (e.g., cathode loading, separator thickness, capacity balance), at 25°C a cell with Li metal and an LLZO solid electrolyte has a heat capacity of ~ 0.7-0.8 J/g-K, while a cell with a graphite anode and a liquid electrolyte has a capacity of 0.9-1.1 J/g-K.[23,24] Of course, observing a temperature rise as high as that shown in **Figure 1.1** is not expected for a variety of reasons (e.g., heat transfer to a cell's surroundings, release of reactants from the cell packaging, the inability of stored electrical energy to be

converted to heat as the cell materials undergo phase changes) but does reflect the higher self-heating potential of cells with higher specific energy and lower heat capacity, as expected of Li metal solid state cells.

Figure 1.1. also indicates the adiabatic temperature rise can exceed the melting temperature of Al and Cu (the typical current collectors), and even the boiling point of Li metal itself.

Thermal safety of a battery is a multi-faceted issue that requires analysis of the (1) onset temperature of self-heating, (2) total heat release, (3) peak temperature, (4) self-heating rate, and other factors such as the release of material from the cell packaging (e.g., toxic gases or reactive materials). As the widespread adoption of Li-ion cells in consumer applications (including automotive) shows, satisfactory safety can be achieved with current Li-ion cells. In this work, we build on experimentally measured calorimetry results and focus on metrics (1) to (4) above.

We note that large differences in these metrics should be expected not only among different liquid electrolyte Li-ion cells (e.g., based on cathode chemistry, cell design), but also among different LiSSB chemistries. As one simple example for expected variation among LiSSB thermal behavior, several oxide solid electrolytes release oxygen when heated (e.g., LATP, LAGP, and LLTO), which will react with adjacent molten Li metal. Calorimetry measurements of these solid electrolytes against molten Li have shown self-heating rates of >10,000 °C/min, which exceeds typical Li-ion thermal runaway peak self-heating rates.[16] In this work we principally focus on the LLZO solid electrolyte, which shows little reactivity against Li metal up

to 300°C, after which, in at least one study, electrolyte discoloration and cracking was observed.[16,25]

Thermal safety concerns become more important as the stored energy density of next generation cells increase, and most established safety tests are designed for the later stages of battery development.[26] Differential scanning calorimetry (DSC) can allow for identification and quantification of thermal safety hazards while on the materials scale level of development to help direct research towards inherently safer materials.

Chapter 2: Modeling Thermal Runaway of a Large Format Lithium Metal All-Solid-State Battery Using Finite Element Method

Introduction

A principal mechanism for self-heating in a Li metal solid state cell with an LLZO solid electrolyte (which is stable against Li metal, and does not release oxygen upon heating up to >400°C), is oxygen release from de-lithiated cathode materials, which typically occurs at around 200 to 300°C, followed by reaction with other cell materials including molten Li. Oxygen released from the cathode that contacts Li will form Li_2O in an exothermic reaction. It is also interesting to note that in a cell with a 1:1 negative capacity to positive capacity (N:P) ratio, the electrochemical discharge of a Li_xCoO_2 cathode has ~25% more energy than the cathode releasing O_2 upon heating, and that O_2 reacting with Li to form Li_2O.[14] O_2 released from the cathode may also react with other cell materials, including conductive carbon, binder, etc. We also note that an advantage of an all-solid-state cell, rather than one in which a solid-state separator is used but a liquid electrolyte is present in the cathode, is that oxygen release from a de-lithiated cathode occurs at a lower temperature (~140°C vs ~ 250°C for $Li_{0.47}CoO_2$, for example) in the presence of a liquid electrolyte than a solid electrolyte such as LLZO.[18,27]

In this work, we used the DSC data measured by Inoue and Mukai of a "microcell" (i.e., an anode, cathode, and separator in a DSC pan) that uses small amounts (~1mg) of $Li_{0.47}CoO_2$, LLZO, and Li to simulate a thermal ramp test as well as short circuit behavior.[15] Placing anode, cathode, and separator materials into a

DSC pan has the advantage of allowing the direct measurement of interactions among cell components upon heating; for example, oxygen release from the cathode and subsequent reaction of that oxygen with molten Li. However, the small sample size introduces challenges associated with achieving mass ratios among cell components reflecting eventual commercial designs, the potential need to prevent electrical shorting through the DSC pan, and DSC calibration. Despite these limitations, this platform provides important insights on the fundamental calorimetry of the materials in a Li metal solid state cell, which in turn provides quantitative information on the four metrics outlined above.

Previous simulations of the thermal behavior of Li-ion cells upon heating, including thermal ramp and oven tests, have been published.[28–31] There are several reactions that take place as a cell is heated from 25°C to >400°C; these reactions have been studied in-depth, and kinetic models have been developed.[19,20,29,32,33] Models of the reactions that take place have been applied to cells and then further expanded to battery packs in order to understand how battery packs may be designed to prevent thermal runaway from spreading[33–36]. While there is extensive work on modeling the thermal behavior of Li-ion cells, there is far less work on LiSSB. There is a need for a significantly expanded set of calorimetry data on the reactions taking place upon heating a LiSSB, as well as the development of kinetic models for those reactions. One recent notable work in this area by A. M. Bates, et. al. provides valuable insight on the expected heat release and adiabatic temperature rise from Li metal cells with all-solid-state cathodes, as well as a range of liquid electrolyte volume fractions in the cathode.[14] They consider a variety of scenarios including whether O_2 released from

metal oxide cathode decomposition can contact molten Li, and they identify this as a critical issue for solid state battery safety. Assuming O_2 and Li metal contact, they find similar adiabatic temperature rise as that shown in **Figure 1.1**. above. This work does not include a model of transient thermal behavior; this is a novel contribution of the present work.

Methods

DSC Data

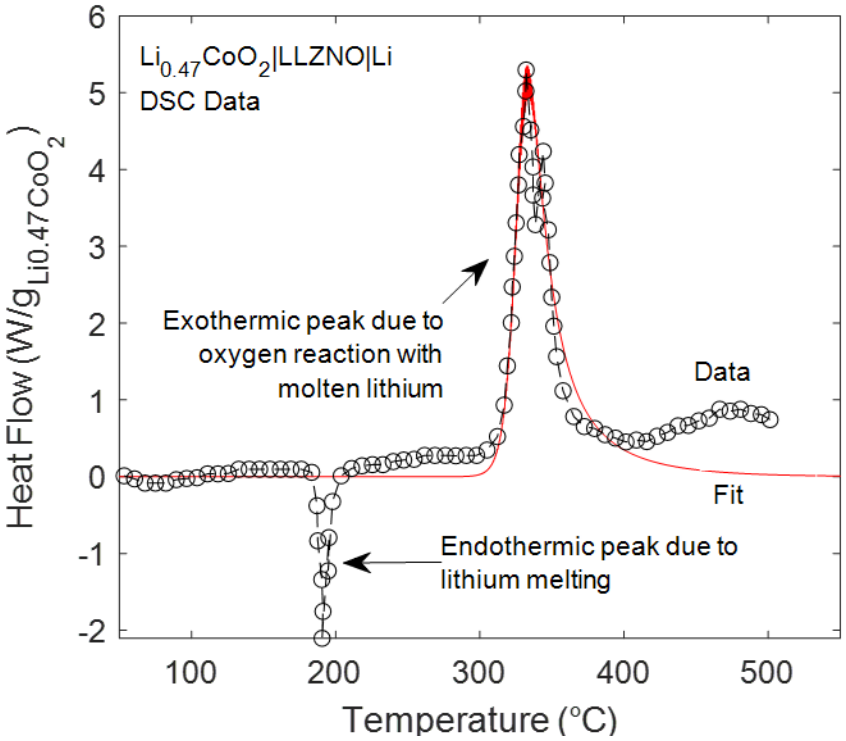

Figure 2.1. Our fit of the exothermic portion of the DSC data obtained by Inoue and Mukai[12] for a $Li_{0.47}CoO_2$|LLZNO|Li microcell at a 5°C/min ramp rate. The endothermic peak associated with the melting of Li melting is handled separately. The dotted line on the experimental DSC data is to guide the eye.

Inoue and Mukai assembled a 1mm diameter $Li_{0.47}CoO_2$ cathode pellet, $Li_{6.75}La_3Zr_{1.75}Nb_{0.25}O_{12}$ (LLZNO) electrolyte pellet, and lithium metal anode inside of a closed stainless-steel pan and electrically isolated the anode and cathode with an alumina tube. This "all-inclusive microcell" was then placed in a DSC and the furnace temperature was ramped to 500°C at a constant rate of 5°C/min.[15] The materials within the microcell progressed through the following reactions:

$$Li(s) \rightarrow Li(l) \tag{2.1}$$

$$Li_yCoO_2(s) \rightarrow yLiCoO_2(s) + \frac{1-y}{3}\ Co_3O_4(s) + \frac{1-y}{3}\ O_2(g) \tag{2.2}$$

$$4\ Li(l) + \ O_2 \rightarrow 2Li_2O(s) \tag{2.3}$$

In addition to their DSC measurements, Inoue and Mukai also collected TGA data on $Li_{0.47}CoO_2$. They found that $Li_{0.47}CoO_2$ begins to release oxygen at ~250°C, with >50% of the oxygen released by 300°C, but the DSC data interestingly does not show an exothermic process beginning until >300°C.[15,27] We hypothesize that the >50°C gap between the temperature at which $Li_{0.47}CoO_2$ releases oxygen, and the temperature at which an exothermic reaction occurs (presumed to be Li_2O formation), is due to passivation of the molten Li by surface layers of Li_2O. The passivation could be achieved, for example, by slow diffusion of O_2 and/or molten Li through a layer of solid Li_2O on the surface of molten Li. Our models in the present work only consider reactions (2.1) to (2.3); as mentioned above, O_2 could also react with other cells components (e.g., conductive carbon), and there may also be additional phase changes (e.g., the melting of Al).

Thermal Ramp Modeling: Domain and Equations

We construct a 2-D transient thermal model of a large-format cell, with the heat source provided by a system of ODEs based on reactions (2.2.1) to (2.2.3) and implement the model in COMSOL. The cell dimensions were set as 30 cm long, 9.8 cm wide, and 1.4 cm tall (reflecting a currently used large-format Li-ion cell, an LG Chem 60 Ah cell). The cell repeat layers include a porous $Li_{0.47}CoO_2$ positive electrode, a LLZO ceramic solid electrolyte, and a lithium metal negative electrode; see **Table 2.3** for more detailed information on the cell parameters. We modeled cells with a 1:1 N:P ratio (i.e., cells with no Li metal at the anode in the fully discharged state). We do not resolve the individual cell layers in our model, but instead use a single domain with spatially averaged properties. The thermal conductivity is anisotropic, as described in more detail below. We assume the cell layers are stacked without any winding.

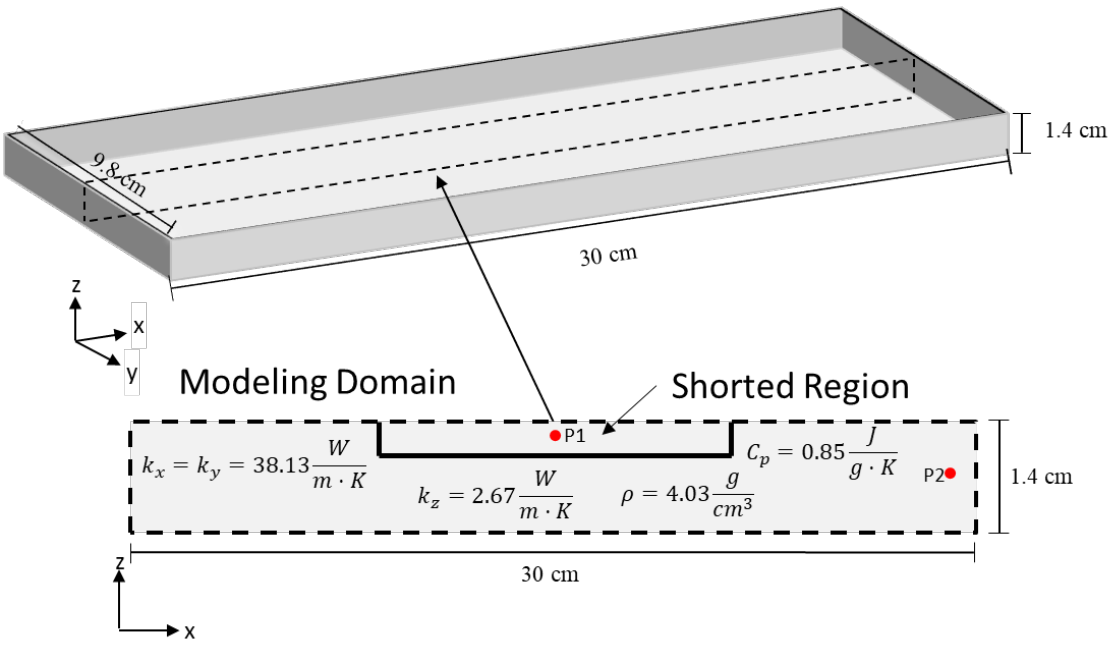

Figure 2.2. Diagram of the 3D cell and the 2D domain that we model. The region labeled "Short circuit" is the region that undergoes shorting in the short circuit model, but in the thermal ramp model behaves in the same way as the rest of the domain. P_1 and P_2 are points referred to in the results section.

A 2D XZ-plane, as seen in **Figure 2.2** is defined as a domain and is meshed with 9000 rectangular mesh elements each with an area of 0.47 mm^2. A scaled relative tolerance of 5×10^{-4} and a scaled absolute tolerance of 5×10^{-7} are used. COMSOL's built in free generalized alpha time stepping method is used. Equation (2.4) is applied to the domain as the governing equation for heat transfer.

$$\rho C_p \frac{\partial T}{\partial t} + \nabla \cdot (-k\,\nabla T) = Q + \frac{q_0}{d_y} \qquad (2.4)$$

An external convective and radiative boundary condition, equation (2.5), is applied to the outer edges of the 2D domain. We also allow for out-of-plane heat

transfer inside of the 2D domain which can occur in either direction, so equation (2.5) is multiplied by 2.

$$q_0 = h_c(T_{ext} - T) + \epsilon\sigma(T_{ext}^4 - T^4) \quad (2.5)$$

We set T_{ext} to ramp at a fixed 5°C/min until 335°C, at which point self-heating is significant, and then keep T_{ext} fixed at 335°C. The internal cell temperature lags T_{ext} because a thermal gradient is developed as heat is transferred into the domain. h_c and ε are kept constant during both the thermal ramp and short circuit simulations.

The thermal conductivity in our model is anisotropic, due to the high thermal conductivity of the current collectors vs. the other cell layers. We assume the cell has layers stacked in the x-y plane, and calculate the thermal conductivity in the z-direction using equation (2.6), and the thermal conductivity in the x and y-directions using equation (2.7).[37]

$$k_z = \frac{\sum \mathrm{h_i}}{\sum \frac{h_i}{k_i}} \quad (2.6)$$

$$k_x = k_y = \frac{\sum k_i h_i}{h_i} \quad (2.7)$$

Perfect contact between the cell layers and the cell casing with no thermal resistance is assumed, allowing the cell casing to be neglected to simplify the domain meshing.

We define a system of ODEs to account for the heat flows in (2.2.1) to (2.2.3) above. The reaction heat flow is applied to equation (2.2.4) through a volumentric heat source as seen in equations (2.8) and (2.2.9).

$$Q = \frac{P}{V} \quad (8)$$

The endothermic melting of lithium is applied to a ±2.5°C range around the melting temperature of lithium. The release of oxygen from the breakdown of $Li_{0.47}CoO_2$ per equation (2.2.2) produces negligible heat and we set the enthalpy of this reaction to zero.[15]

$$P = \Delta H_{Li_2O} n_{0,LCO} \frac{dx_{Li_2O}}{dt} + \Delta H_m \frac{dn_{Li,melt}}{dt} \quad (2.9)$$

The decomposition of Li_yCoO_2 in equation (2.2.2) is modeled with an Arrhenius rate equation shown in equation (2.2.10) that has been previously paramaterized in literature.[19,20] We set the Li_2O reaction as second order, depending on the mole fractions of O_2 and Li. The rate coefficient, κ and Heaviside functions in equations (2.2.13) and (2.17) is adjusted so the heat flow matches that seen in the DSC data in **Figure 2.1.** The rate equations for Li and O_2 are written as a combination of the rate equations for Li_yCoO_2 and Li_2O.

$$\frac{dx_{LCO}}{dt} = -Ae^{\frac{E_a}{RT}} x_{LCO}^{1.62} \quad (2.10)$$

$$\frac{dx_{Li}}{dt} = -2\frac{dx_{Li_2O}}{dt} \quad (2.11)$$

$$\frac{dx_{O_2}}{dt} = -0.176\frac{dx_{LCO}}{dt} - 0.5\frac{dx_{Li_2O}}{dt} \quad (2.12)$$

$$\frac{dx_{Li_2O}}{dt} = H(T)\kappa x_{Li} x_{O_2} \quad (2.13)$$

Again, this reaction system is directly parameterized to the DSC data in **Figure 2.1.**, so that the total amount of heat, the onset temperature, and the heat rating have a physical basis. The most important aspect of this parameterization to the DSC data is the fact that while TGA shows O_2 release from $Li_{0.47}CoO_2$ at ~250 °C, the

DSC shows no significant exotherms until >300°C.[15,38] This indicates molten Li is present with O_2 but there is no reaction until the temperature in the DSC exceeds 300°C. We account for this behavior with the $H(T)$ function in equation (2.2.13). We provide a possible a physical basis for this gap in **Figure 2.3**; in particular, O_2 released from the cathode may react with molten Li to form a layer of solid Li_2O that slows the reaction. As the temperature rises, a "breakthrough" of this layer occurs such that unreacted molten Li and O_2 react more quickly. This type of behavior has been previously reported in studies of Li metal reactivity with various gases and requires further study.[39]

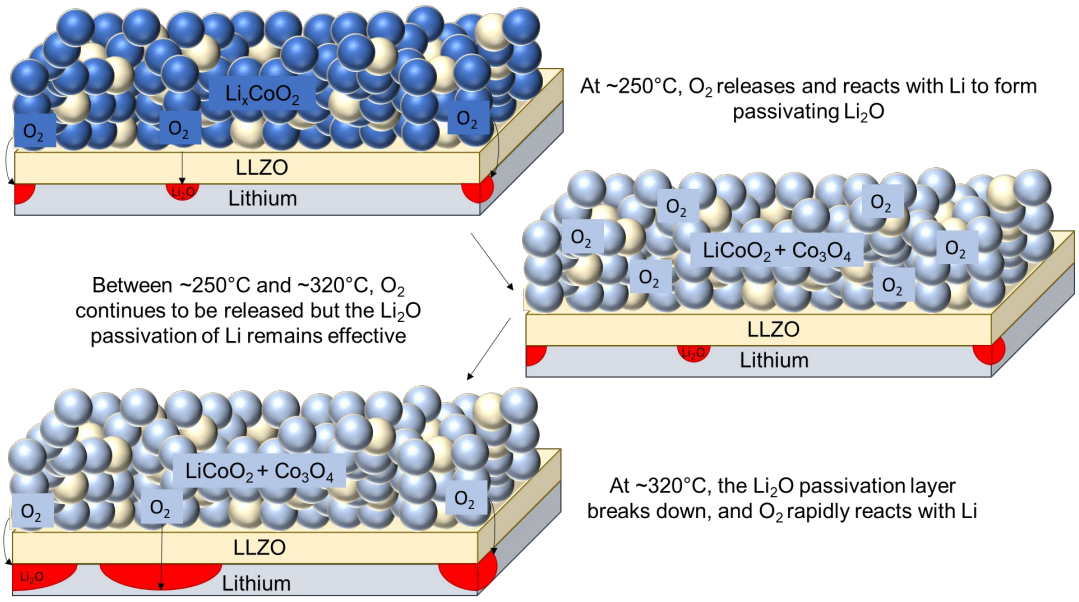

Figure 2.3. Schematic of the potential reaction sequence of molten Li with O_2 gas.

Short Circuit

While thermal ramp is a common safety test, short circuit is also of great interest due to the potential for cell penetration or manufacturing defects. If an

internal or external electrical short takes place, the cell will self-discharge and generate heat. While there have been sophisticated models developed to treat the coupled thermal and electrochemical behavior that occurs during a short circuit[40–43], here we use a simplified approach. The goal of this model is to provide a basic treatment of the coupling between self-discharge (which depletes the amount of reactant for thermal reactions) and heat transfer within the cell and to the surroundings. In particular, we model a constant-current short and assumed a fixed cell potential to obtain a self-heating rate. Rather than short the entire cell, we define a short in a portion of the cell, as shown by the label "Short Circuit" in **Figure 2.2**. Additional details on our shorting model are provided in

Table 2.4. T_{ext} was set to a constant 25°C.

Equations (2.10) and (2.11) were modified to include a short circuit term that accounts for the electrochemical reaction of Li and $Li_{0.47}CoO_2$, as shown in equations (2.14) to (2.17). In our model we allow the electrochemical self-discharge to continue past lithium melting. The short circuit reaction stops when all $Li_{0.47}CoO_2$ is consumed. Note that $Li_{0.47}CoO_2$ can be reacted either electrochemically due to self-discharge, or due to thermal decomposition, as shown in equation (2.2.14). Oxygen release is only due to $Li_{0.47}CoO_2$ thermal decomposition.

$$\frac{dx_{LCO}}{dt} = -x_{LCO,0}\frac{I}{C}H(x_{LCO}, x_{Li}) - Ae^{\frac{E_a}{RT}}x_{LCO}^{1.62} \quad (2.14)$$

$$\frac{dx_{Li}}{dt} = -x_{Li,0}\frac{I}{C}H(x_{LCO}, x_{Li}) - 2\frac{dx_{Li_2O}}{dt} \quad (2.15)$$

$$\frac{dx_{O_2}}{dt} = 0.176Ae^{\frac{E_a}{RT}}x_{LCO}^{1.62} - 0.5\frac{dx_{Li_2O}}{dt} \quad (2.16)$$

$$\frac{dx_{Li_2O}}{dt} = H(T)\kappa x_{Li} x_{O_2} \quad (17)$$

We use a short circuit current corresponding to a 30C discharge rate (i.e., 2 minutes), which is an important sensitivity for this model. The equation for the heat generation rate for this short-circuiting case is modified to include two terms, one for the heating associated with electrochemical shorting, and the second for the reactions that occur as the temperature rises, as shown in equation (2.18). Equation (2.18) includes bounding functions to improve numerical stability.

$$P = \Delta G_{ave} n_{0,LCO} \frac{I}{C} H(x_{LCO}, x_{Li}) + \Delta H_{Li_2O} n_{0,LCO} \frac{dx_{Li_2O}}{dt} + \Delta H_m \frac{dn_{Li,melt}}{dt} \quad (18)$$

$$\Delta G_{ave} = -nFV_{cell,ave} \quad (19)$$

Results and Discussion

Thermal Ramp

Figure 2.4. shows results from our thermal ramp model. Panel a) shows the transient profiles of the components in our model, as well as the cell temperature at a point P_{TR}. Panel b) provides a more detailed look at the time window in panel a) with the highest reaction rates. Panel c) shows the 2D temperature distribution and 2D heat flow profile when the reaction rates are highest, and Panel d) shows the 2D temperature distribution at the maximum temperature at P_{TR}. There are several important points in **Figure 2.4**. In panel a), at P_{TR} lithium begins to melt at 62.75 minutes when the temperature reaches ~180°C. Li melting slows down the temperature rise for ~4 minutes. At points near the cell surface, lithium melts at 61.75

minutes. $Li_{0.47}CoO_2$ begins to decompose at ~72 minutes when the cell reaches 200°C, however the rate of decomposition rises when P_{TR} reaches 250°C following equation (2.2.2). O_2 released from $Li_{0.47}CoO_2$ does not react with molten lithium until P_{TR} reaches ~320°C, at which point the formation of Li_2O rapidly occurs and the cell enters thermal runaway.

The heat from the oven enters the outside of the cell, so the thermal runaway moves from the outside to the inside of the cell. However, the highest temperature and heating rate occur in the center of the cell, at P_{TR}, because that point is furthest from the walls. The anisotropic thermal conductivity results in thermal runaway moving faster in the x-direction than the z-direction, as shown in **Figure 2.4**.d). The maximum heat flow is 5.85 W/g which is similar to the DSC experiments conducted at the same temperature ramp.[15] At the end of thermal runaway, at P_{TR} a maximum temperature of 1029°C is seen. This is higher than maximum temperatures observed in many liquid electrolyte Li-ion cells, although this depends on several assumptions in our model, including the cutoff temperature of the oven.[28,44,45] A later section describes our model assumptions and limitations in more detail.

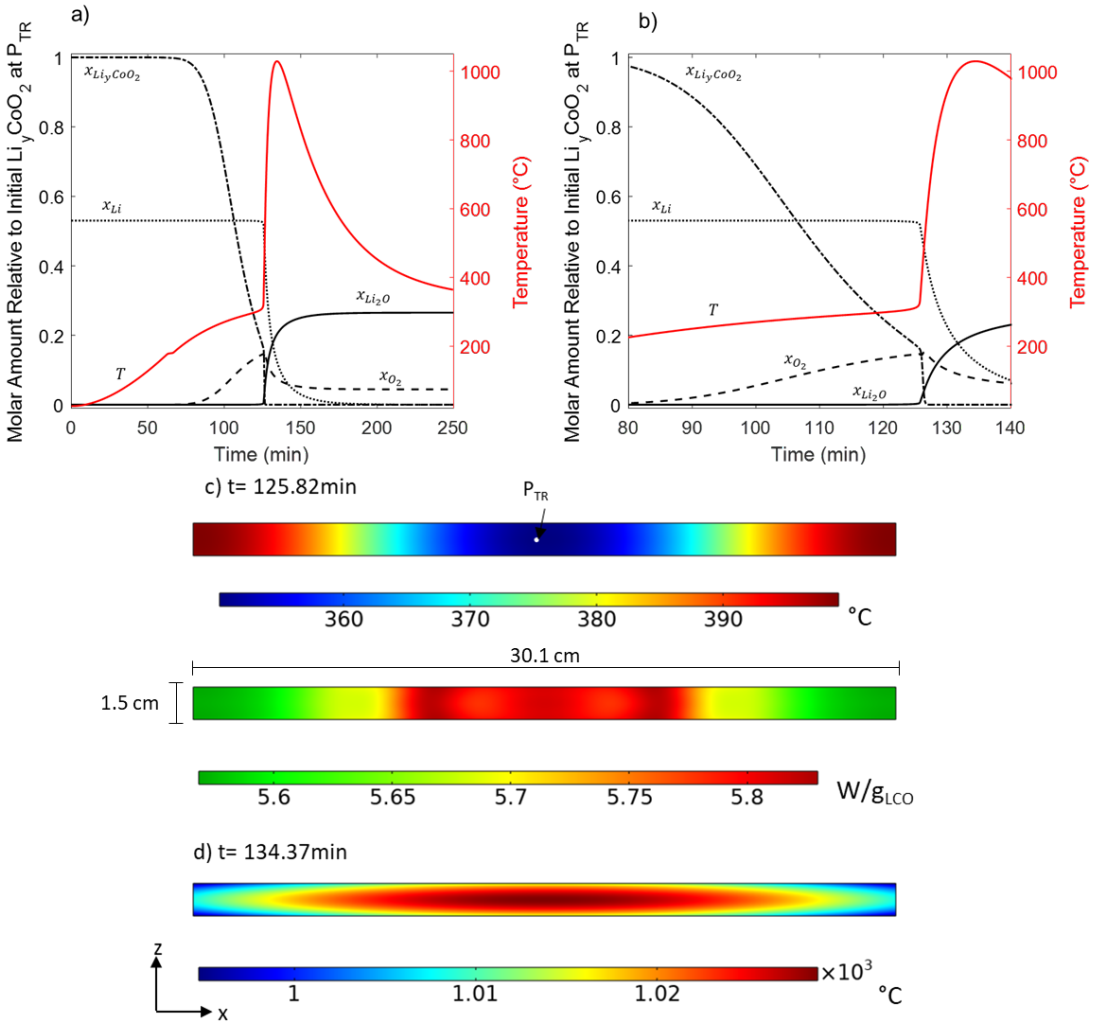

Figure 2.4. Thermal ramp model results. a) The molar ratios (vs. initial moles of $Li_{0.47}CoO_2$) and temperature at point P_{TR} b) the same quantities during the thermal runaway stage of the simulation c) 2D temperature (top) and 2D heat flow (bottom) profiles at 125.82 minutes, when heat flow is highest and d) the 2D temperature profile at the peak temperature at 134.37 minutes

We also note the importance of the initial cell negative to positive capacity ratio in the evolution of both the mole ratios and heat produced. For an initial lithiation state of $Li_{0.47}CoO_2$ and a 1:1 N:P ratio, O_2 is in excess, and about 0.05 moles of oxygen per mole of $Li_{0.47}CoO_2$ remain after thermal runaway, as **Figure 2.4.**

shows. This corresponds to ~25% of the total O_2 released from $Li_{0.47}CoO_2$. Cells with more Li than required for a 1:1 N:P ratio will demonstrate more heat generation as more oxygen is consumed; in particular, with Li in excess the heat release from Li2O formation would rise by ~25%.

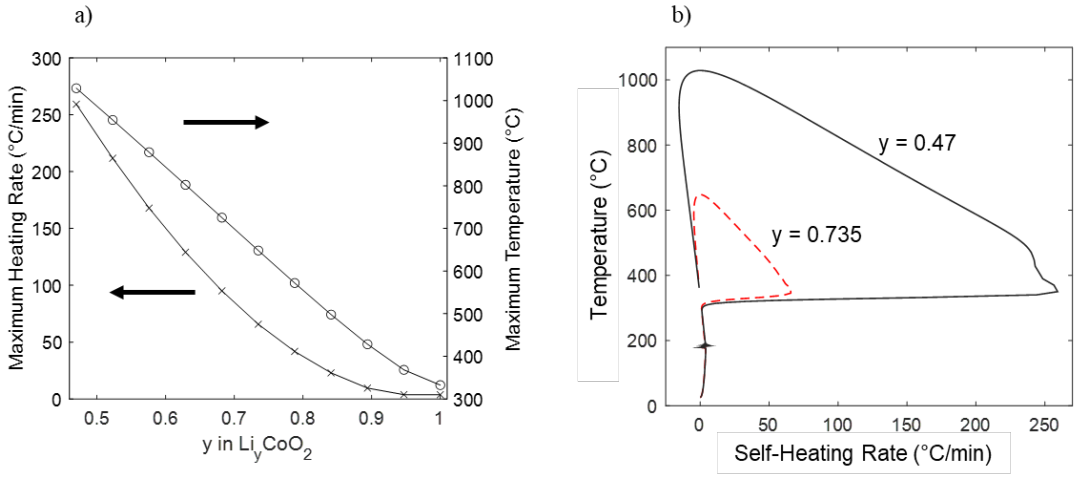

Figure 2.5. Thermal ramp model results at P_{TR}. a) the maximum heating rate and maximum temperature for different initial Li_yCoO2 and b) temperature vs. heating rate for lithiation states corresponding to 100% and 50% states of charge.

The next important result from our thermal ramp modeling is shown in **Figure 2.5.** Panel a) shows the maximum self-heating rate and temperature as functions of y in Li_yCoO_2 (i.e., initial SOC). Panel b) shows the temperature vs. the heating rate for values of y in Li_yCoO_2 corresponding to 50% and 100% SOC. These panels show that the heating rate and maximum temperature both increase as the initial cathode lithium content falls (i.e., the SOC rises) In panel a), there is a nearly linear relationship between lithiation state and maximum temperature. Note that as $y \rightarrow 1$ the linear relationship breaks down; when no exothermic reactions occur the maximum temperature is just that of the oven. However, the maximum heating rate is

flatter as $y \to 1$. For example, in panel b) we see the maximum heating rate at a lithiation state of 0.735 (50% SOC) is ~25% that of the maximum heating rate at a lithiation state of 0.47 (100% SOC).

As the SOC of the cathode decreases, the amount of lithium initially present and the amount of oxygen produced both fall linearly. Hence, oxygen remains in excess at all states of charge, so the total heat generated is also linear with the state of charge. However, the maximum heating rate depends on both the total heat produced as well as thermal transport, and at lower SOCs the thermal transport results in a lower heating rate. [18,28,33]

Short Circuit

Figure 2.6. shows results from our short circuit model. Panel a) in **Figure 2.6.** shows the temperature and mole ratios at point P_1, as defined in **Figure 2.2.** As shown in this panel, the short results in reductions in $x_{LiyCoO2}$ and x_{Li} due to electrochemical production, as well as strong heat production as all electrochemical energy is converted to heat. At ~0.6 minutes, the shorted region reaches 250°C at which point O_2 release from the $Li_{0.47}CoO_2$ begins. After this point, the self-discharge and thermal decomposition processes both consume $Li_{0.47}CoO_2$. Even after $Li_{0.47}CoO_2$ is fully consumed within the shorted domain, heat release continues as O_2 and Li react to form Li_2O and the temperature continues to rise. Panel b) shows the first 6 minutes of panel a). Here Li melting be seen at ~0.42 minutes when the temperature rise briefly slows. There is also a notable change in slope at ~1.2 minute and ~1.6 minutes. The slower temperature rise between 1.2 and 1.6 minutes occurs because

the electrochemical short is complete and the kinetics of Li_2O formation are slower; the increase in the temperature slope at 1.6 min is due to heat from outside the shorted region heating the shorted region. Panel c) shows the temperature profile and molar ratios at P_2, as defined in **Figure 2.2.** This is the location where the maximum temperature is reached. At this point and at every point outside of the short region, the temperature rise is due to thermal transport from the shorted region which causes sufficient temperature rise (i.e., to >320°C) to cause thermal runaway. The peak temperature at P_2 is 965°C and the maximum heating rate is ~600°C/min. The lower maximum temperature and heating rate are due to the T_{ext} fixed at 25°C in the short circuit model, vs. the rising oven temperature in the thermal ramp model. Panel d) shows the first 6 minutes of panel c). Here, the melting of lithium can be seen in the temperature profile at 3.15 minutes, and the decomposition of Li_yCoO_2 happens between ~3.5 and 4.5 minutes. The temperature difference between P_1 and P_2 is as high as 450°C; this occurs at 1.5 minutes. When P_2 reaches its maximum temperature, the temperature difference between P_1 and P_2 is ~130°C.

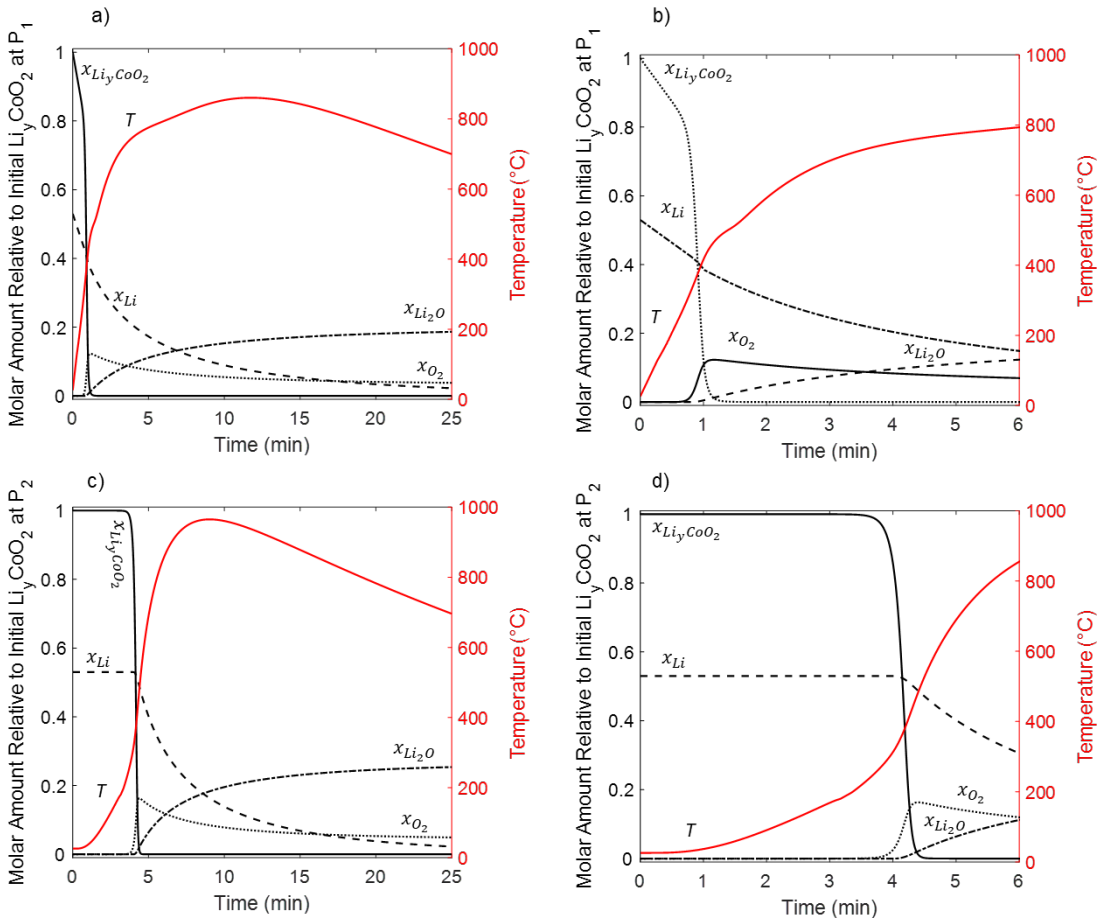

Figure 2.6. Short circuit model results showing the temperature and molar ratios vs. initial $Li_{0.47}CoO_2$ at a) P_1, a point within the short circuit b) P_1 during the first 6 minutes c) P_2, a point on the right edge of the cell where there is no shorting and d) P_2 during the first 6 minutes.

Figure 2.7. shows the 2D temperature distribution at three time points. Panel a) shows the time (1.5 minutes) when thermal runaway is occurring within and in the immediate surroundings of the short circuit region, panel b) shows the time (5.5 minutes) when thermal runaway has spread to the rest of the cell, and panel c) shows the time (9 minutes) when the maximum temperature in the cell is reached. At 9

minutes the heat flow at P_1 is 2% of the maximum heat flow at that point, and the heat flow at P_2 is 17% of the maximum heat flow at that point.

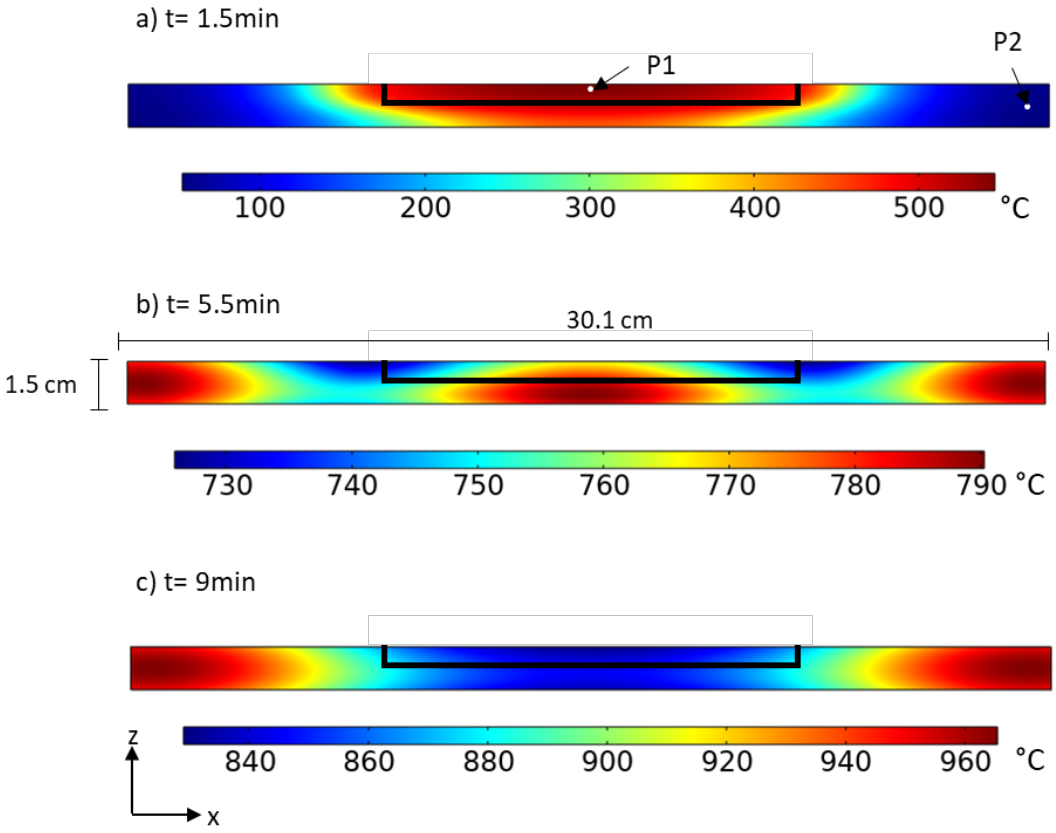

Figure 2.7. Two-dimensional temperature profiles for the short circuit model at three times. a) 1.5 min, when heating is concentrated in the shorting region b) 5.5 min, when heat from the shorted region has caused thermal runaway in the rest of the cell, and c) 9 min, when the maximum temperature is reached.

For the 2-minute discharge rate in the shorted region chosen here, as well as the size of the shorted region, the heat produced in the shorted region is sufficient to induce thermal runaway throughout the entire cell. For a higher shorting rate, the maximum temperature would be higher than what is seen here, while if the shorting rate is small enough thermal runaway may never occur in the cell, as the rate of heat

transferred to the environment would keep all cell regions at <320°C. Similarly, a larger shorted region would be more likely to induce thermal runaway in the rest of the cell than a smaller shorted region, for a fixed shorting rate.

Important Model Assumptions and Sensitivities

There are a variety of important assumptions in this model. First, there are several processes that are not included, including the melting of Al (660°C), heat flows associated with cell packaging, any heat flows associated with cell materials not captured in the DSC data we are using (which ran to 500ºC and did not include PVDF, conductive carbon, or current collectors), gas venting from the cell, gas ingress to the cell (e.g., due to rupture), molten Li exiting the cell or moving within the cell, O_2 gas moving within the cell, and the temperature dependence of some of the materials (see **Table 2.2.**). Regarding the DSC data we use only being collected to 500°C, we do note that the principal exothermic reactions (i.e., O_2 released from the cathode reacting with cell components) take place at <500°C, and we do not expect any major exothermic reactions that only occur at >500°C. Another key assumption is the functional form we choose for Li_2O formation (Equation 2.17). As discussed above, we hypothesize that the difference in the temperatures between when O_2 is released and when the exotherm for Li_2O occurs is due to a passivating layer of Li_2O on the molten Li; this is an area that requires further study. The function we use here to fit the observed thermochemistry of Li_2O formation in a DSC pan may be different in a large-format cell. We also assume that O_2 cannot move among cell regions; in other words, O_2 can only be consumed where it is generated.

Our model also assumes that the kinetic expressions we developed to fit the DSC data collected at 5°C/min are valid at other heating rates, including the 100s °C/min we observe in both the thermal ramp and short circuit tests. Finally, the present short circuit model assumes a fixed shorting current within a pre-defined spatial domain, while in practice shorting is likely to have strong spatial and temporal variations.

In addition to these assumptions, there are also several important model inputs that affect the model results that we discuss further in Chapter 3. These include the thermal boundary conditions (here all cell surfaces have the same heat transfer properties, while in a battery pack the cell surfaces could have significantly different thermal boundary conditions), the cell specific energy, the cathode and separator materials, the absence of any conductive additive or binder, and, for the short circuit model, the rate of the short.

Conclusions

While LiSSB are not subject to the reactions associated with organic solvent liquid electrolyte, the oxygen released from a metal oxide cathode may react with molten Li or other cell components and lead to significant heat release and cell temperature rise, potentially requiring cell and pack engineering to mitigate safety concerns unless either the O_2 gas or the molten Li can be removed from the cell. Building on previously reported direct DSC measurements of the heat flows associated with one LiSSB chemistry (Li|LLZO|Li_yCoO_2), we have constructed a 2D thermal model of a large-format cell that quantifies important thermal behaviors including the maximum temperature, maximum heating rate, and onset temperature

for heat release. We considered both a thermal ramp, as well as a case in which a subset of the cell shorted, which led to sufficient heating to put the entire cell in thermal runaway. For the thermal ramp test, the onset temperature was ~300ºC, the peak temperature ~1030ºC, and the maximum heating rate ~250ºC/min. It is worth nothing that while the cell in our model does not reach the melting point of copper (1085°C) or the boiling point of lithium (1342°C), those values may potentially be reached. While the peak temperature and maximum heating rates here are comparable to those reported for some high-energy Li-ion cells,[22,40,44,45] the onset temperature for self-heating is substantially higher than for Li-ion, where self-heating can begin at <100ºC.[10,11,46,47] This is a principal first advantage for solid-state cells without liquid electrolyte. Our short circuit model showed a similar peak temperature to the thermal ramp, and a ~2.2x higher maximum heating rate. For both the thermal ramp and short circuit tests, the peak temperature is ~50% of that resulting from adiabatic thermal boundary conditions; methods to slow the exothermic $Li+O_2 \rightarrow Li_2O$ reaction could reduce this value. The heating rate has a strong influence on the peak temperature; the higher the heating rate, the higher the peak temperature as there is less heat release to the surroundings.

A key insight of the present work, also reflected in the recent work of A. M. Bates, et. al., is that managing the contact of molten Li metal (or other cell components that may be oxidized in an exothermic reaction) with oxygen released from the cathode is of critical importance for the thermal behavior of LiSSB.[14] A separator that maintains an effective barrier between Li and oxygen even as a cell heats in an oven test may substantially reduce self-heating reactions from occurring.

This could likely be facilitated in practice by venting oxygen produced from cathode breakdown from the cell, although removing O_2 gas from within a solid-state cell stack in which the layers are typically pressed together introduces challenges. Another important insight of this work is that for a LiSSB that heats due to internal shorting, the kinetics of continued shorting and heating (even after Li melts) vs. oxygen release from the cathode (which consumes delithiated cathode material) and subsequent Li_2O formation will be of critical importance for the ultimate heating rate and peak temperature. At present there is little empirical understanding of how these processes may occur within a large-format LiSSB stack that may be under modest compression (e.g., 1 MPa). Future work will explore key model assumptions and sensitivities.

Model Parameters and Additional Functions

Table 2.1. Table of Symbols

Symbol	Definition
T	Cell temperature
ρ_i	Density of species *i*
$C_{p,I}$	Specific constant pressure heat capacity of species *i*
h_c	Heat transfer coefficient
Q	Volumetric heat from reaction and phase change
q_0	Heat transferred to or from the surroundings
ϵ	Emissivity
σ	Stefan-Boltzmann constant
T_{ext}	External temperature
k_x	Average thermal conductivity in the x-direction
k_z	Average thermal conductivity in the y-direction
k_i	Thermal conductivity of species *i*
h_i	Thickness of cell layer *i*
P	Summation of heat from exothermic reaction, endothermic melting, and electrochemical discharge
x_{LCO}	Mole fraction of Li_yCoO_2 relative to initial moles of Li_yCoO_2
x_{Li}	Mole fraction of Li relative to initial moles of Li_yCoO_2
x_{O_2}	Mole fraction of O_2 relative to initial moles of Li_yCoO_2
x_{Li_2O}	Mole fraction of Li_2O relative to initial moles of Li_yCoO_2
$H(i)$	Heaviside function dependent on variable i
ΔG_{ave}	Gibbs free energy of an electrochemical cell
n	Number of moles of electrons transferred in electrochemical discharge per mole of cathode active material
F	Faraday's Constant
$V_{cell,ave}$	Nominal voltage of cell discharge
I	Short circuit current
C	Cell capacity
ΔH_{Li_2O}	Enthalpy of $Li+O_2 \rightarrow Li_2O$ reaction
$\Delta H_{m,Li}$	Enthalpy of lithium melting
$n_{Li,melt}$	Number of moles of melted Li metal. Note that this variable is used solely for heat of lithium melting and is separate from x_{Li}
d_y	Length of the out-of-plane direction (the y-direction in our model)

Table 2.2. Material Properties

Parameter	Value	References and notes
k_{LLZO}	$0.47\ \frac{W}{K \cdot m}$	[48]
k_{LCO}	$3.7\ \frac{W}{K \cdot m}$	[49,50]
$k_{Li,s}$	$84.7\ \frac{W}{K \cdot m}$	[21,51]
$k_{Li,l}$	$44.5\ \frac{W}{K \cdot m}$	[21,52]
k_{Al}	$237\ \frac{W}{K \cdot m}$	[51]
k_{Cu}	$401\ \frac{W}{K \cdot m}$	[51]
ρ_{LLZO}	$5.11\ \frac{g}{cm^3}$	[53]
ρ_{Li}	$0.534\ \frac{g}{cm^3}$	[21,51]
ρ_{LCO}	$5.1\ \frac{g}{cm^3}$	[53,54]
ρ_{Al}	$2.70\ \frac{g}{cm^3}$	[51]
ρ_{Cu}	$8.96\ \frac{g}{cm^3}$	[51]
$C_{p,Li}$	$3.582\frac{J}{g \cdot K}$	[21,51]This value is for 25°C
$C_{p,LCO}$	$0.67\ \frac{J}{g \cdot K}$	[24,55,56]This value is for Li_1CoO_2 at 25°C
$C_{p,LLZO}$	$0.68\frac{J}{g \cdot K}$	[57]This value is for 25°C
$C_{p,Al}$	$0.897\ \frac{J}{g \cdot K}$	[51]This value is for 25°C
$C_{P,Cu}$	$0.385\ \frac{J}{g \cdot K}$	[51]This value is for 25°C
$T_{melt,Li}$	$180.5°C$	[21,51]

Table 2.3. Averaged Cell Parameters

Parameter	Value	Reference/Notes
Cathode thickness	80 μm	
Anode thickness	20.7 μm	
Electrolyte thickness	10 μm	
Al and Cu Current Collector Thicknesses	5 μm	
Cathode Active Material Volume Fraction	0.70	
k_{xx}	38.04 $\frac{W}{K \cdot m}$	
k_{zz}	2.67 $\frac{W}{K \cdot m}$	
ρ_{total}	4.03 $\frac{g}{cm^3}$	
$C_{p,average}$	0.84 $\frac{J}{g \cdot K}$	Averaged from temperature dependent material heat capacities across the expected temperature range
h_c	7.17×10^{-4} $\frac{W}{cm^2 K}$	[29]
σ	5.669×10^{-12} $\frac{W}{cm^2 K^4}$	
ϵ	0.04	
Specific Energy	355 $\frac{Wh}{kg\ cell\ repeat\ layers}$	For a 4.05V average discharge voltage starting from $Li_{0.47}CoO_2$
Energy Density	1493 $\frac{Wh}{L\ cell\ sandwich}$	For a 4.05V average discharge voltage starting from $Li_{0.47}CoO_2$
κ	0.0129	
T_{react}	330°C	
A	$3.76 \times 10^8\ s^{-1}$	[20]
E_a	1.14×10^5 $\frac{J}{mol}$	[20]
H_1	432.21 $\frac{J}{g\ Li}$	
H_2	-2200 $\frac{J}{g\ LCO}$	
$n_{LCO,0}$	10.68 mol	
$n_{Li,0}$	5.66 mol	
C	88.7 Ah	

I	2662 A
n	0.53
d_y	9.8 cm

Table 2.4. Additional Functions

Function	Expression	Notes
$H(T)$	$\kappa\,(0.5 + 0.5\tanh(0.1(T - T_{react}))$	Suppresses Li_2O formation until the reaction temperature for numerical stability and fitting to experimental heat flow data.
$H(x_{LCO})$	$0.5 + 0.5\tanh(10^5(x_{LCO} - 0.01))$	Cuts off the short circuit when Li_yCoO_2 is no longer available and only $LiCoO_2$ remains.
$H(x_{Li})$	$0.5 + 0.5\tanh(10^5(x_{Li} - 0.01))$	Cuts off the short circuit when Li is no longer available. $H(x_{LCO})$ will reach zero before this function, so this is used for redundancy.

Acknowledgements

This is the preprint manuscript version of an article published in the Journal of the Electrochemical Society. IOP Publishing Lt is not responsible for any errors or omissions in this version of the manuscript or any version derived from it. The Version of Record is available online at Johnson, N. B.; Albertus, P. Modeling Thermal Behavior and Safety of Large Format All-Solid-State Lithium Metal Batteries under Thermal Ramp and Short Circuit Conditions. *J. Electrochem. Soc.* **2022**, *169* (6), 060546. https://doi.org/10.1149/1945-7111/ac79cf

Chapter 3: Sensitivity Testing of Large Format All-Solid-State Lithium Metal Battery Thermal Safety Model

Introduction

We previously modeled a thermal ramp test and short circuit of a theoretical large format LiSSB using differential scanning calorimetry heat flow data for an "all-inclusive microcell."[15] We found that while the LiSSB thermal runaway onset temperature is significantly higher than Li-ion (250°C compared to ~100°C), the peak temperature and maximum heating rate are comparable. Our published work on this model only used one set of parameters and did not explore reasonable variations in parameters. While some of these values, such as the averaged thermal properties, cannot be varied independently, other properties like the environmental heat transfer boundary conditions and cell design characteristics can be varied independently for a sensitivity analysis. In this work, we analyze the sensitivity of our thermal runaway model to various parameters like κ, the specific energy, and the convective heat transfer coefficient bounded within a physically reasonable range of values.

Sensitivity Testing Methods

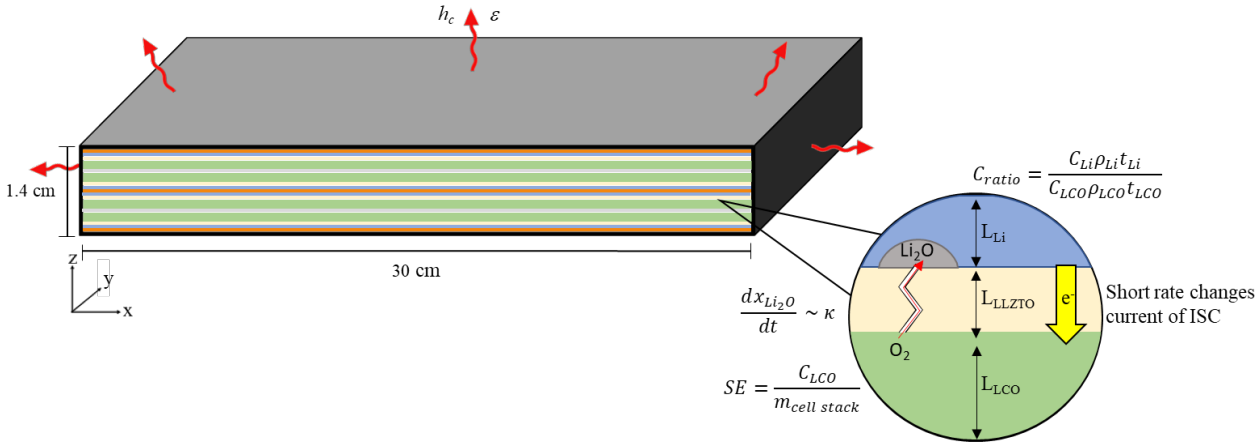

Figure 3.1. Diagram of the theoretical large format cell. We vary 1) k which corresponds to transport limitations imposed by the integrity of the LLZO separator and initial Li_2O formation, 2) the heat transfer coefficient, 3) the thicknesses of the layers to vary specific energy, 4) the thickness of the anode to vary N:P ratio, and 5) the short rate specifically in the short circuit model.

To test the model sensitivity to important parameters, we vary the convective heat transfer coefficient, radiative emissivity, specific energy, N:P ratio, and κ coefficient on both the short circuit and the thermal ramp models for the models shown in the previous chapter. Specifically on the short circuit model, we also vary the short rate. We determine the sensitivity of each parameter in the thermal ramp by comparing the maximum temperature and maximum heating rate at the center point of the 2D domain. We chose the center point as this is the location with the highest temperature in the cell. We determine the sensitivity for the short circuit by comparing the maximum temperature and heating rate at P_1 and P_2 shown in **Figure 2.2.** We chose these points because P_1 sees the highest temperature inside of the short circuit, and P_2 sees the highest temperature outside of the short circuit. We average the thermal properties of the cell layers rather than explicitly defining and meshing

each individual layer to reduce computational costs. As the cell composition changes, particularly for the specific energy and N:P ratio sensitivity analysis, the average thermal properties of the cell change accordingly. This is an important consideration when evaluating the sensitivity of the model with specific energy and N:P ratio as there are multiple cell parameters changing at once.

When deciding which values should be swept for each parameter, we bound the upper and lower limits for each of these parameters to values that are physically reasonable. For h_c, we vary between the estimated free convective heat transfer coefficient of air (5 W m^{-2} K^{-1}) and an estimated forced convective heat transfer coefficient of a glycol/water flow (145 W m^{-2} K^{-1}). Nelson et. al. estimate the convective heat transfer coefficient of a glycol/water coolant system by the Nusselt Number, Graetz Number, Reynolds number, and Prandlt number to be ~350 W m^{-2} K^{-1}, however this estimation varies with design considerations of the coolant system.[58] For emissivity, we vary the parameter between 0.05 and 0.9. We use 0.9 as an upper limit for an estimate of emissivity for aluminum painted black. The default value we use is 0.04 which is the emissivity of mylar used in pouch cell construction. To vary specific energy, we change the layer thickness of the anode, cathode, and electrolyte. The most important layer thickness to change to increase the specific energy for this LCO|LLZO|Li large format cell was the electrolyte thickness due to the high density of LLZO (5.1 g/cm^3). We use a similar approach to vary the negative to positive electrode capacity ratio (N:P ratio) by changing the thickness of the lithium metal anode relative to the cathode. Our default setting is to use capacity matched electrodes (N:P ratio of 1) in the charged state which corresponds to a cell without Li

in the discharged state. At higher N:P ratios, lithium would have to be present in the fully discharged state. We vary the N:P ratio from 0.8 to 1.3 to look at the safety of an LiSSB after irreversible capacity loss occurs (N:P ratio < 1) and to look at cases where excess lithium is included (N:P ratio > 1). Lastly, to physically bound κ, we use the total reaction time for Li_2O formation in the model as κ is more of a phenomenologically fitted value that encompasses the kinetic frequency factor as well as transport limitations than a property. Lithium heated to a molten form with a flame and then left to react in air demonstrates a sustained exothermic reaction over the timespan of 10s of seconds to 10s of minutes. We use κ values that result in the model showing reaction occurring in a total amount of time inside of that timeframe. Higher κ values correspond to less transport limitations and/or faster reaction kinetics. This could be as a result of higher surface area to volume ratios of the lithium metal anode, more cracks and imperfections in the LLZO allowing for more diffusion of oxygen, higher porosity in the Li_2O surface layer, or faster reaction kinetics. The lower the κ value, the more transport and kinetic limitations are imposed on Li_2O formation.

Results and Discussion

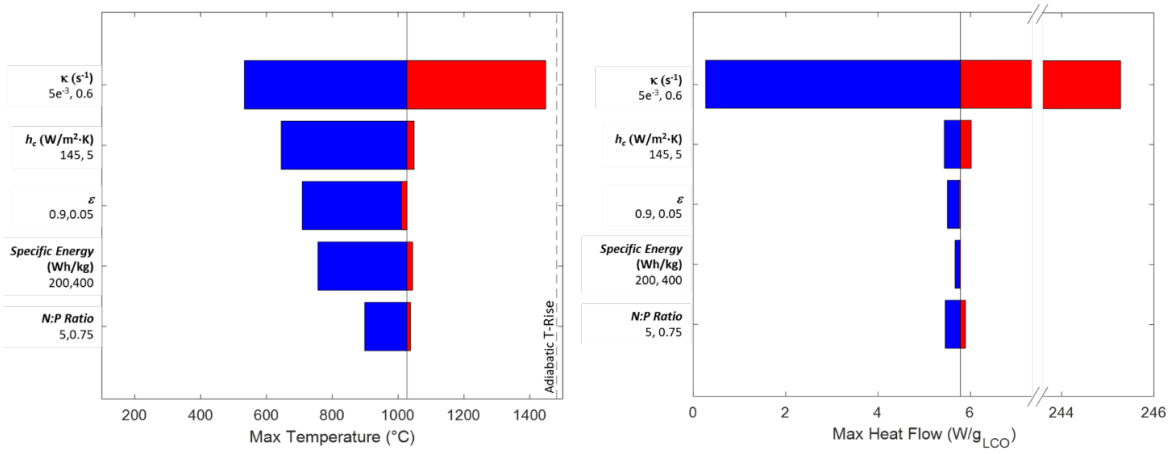

Figure 3.2. Thermal ramp tornado plots showing the variation in a) maximum temperature with changing parameter values and b) maximum heat flow with changing parameter values. The two quantities underneath each parameter on the y-axis correspond to the low value and the high value for each parameter tested.

The base values for the maximum temperature rise above the oven temperature and maximum heating rate in the thermal ramp are 1027°C and 5.78 W/g_{LCO} respectively. All the tested parameters, excluding κ, do not increase the maximum temperature observed by >1%, with the increase of 9°C above the base value for h_c being the largest increase in the maximum temperature. These parameters have a much larger effect on decreasing temperature with h_c, ε, and specific energy all showing a >200°C reduction in the maximum temperature relative to the base value. We are already within 400°C of the adiabatic temperature rise with the base case, so any increase in heat flow or reduction in heat dissipation will have diminishing returns on the maximum temperature. Conversely, increasing the heat dissipation or reducing the heat flow will have a substantially higher impact on reducing the

maximum temperature. The two ways in which the maximum temperature will increase the most are to either increase the total amount of heat generated, or to increase the rate of heat release. The convective heat transfer coefficient and emissivity only remove heat from the system as it's generated. Decreasing them further than what is seen in the base case does little to increase the maximum temperature, because the rate of self-heating is so high. In the case of N:P ratio and specific energy, the thicknesses of the cell stack layers are changing along with the total amount of heat generated. Despite the total heat increasing, the changing thermal properties keep the maximum temperature from increasing more than 21°C above the base case. While increasing the emissivity to 0.9 lowers the maximum temperature to 709°C, this will not be very useful in a commercialized battery pack. Emissivity is important for a thermal ramp test where a single battery sits in an oven, but there should be little to no radiative heat transfer in a tightly packed battery pack with prismatic cells as aluminum cooling plates will conduct heat away from the cell surface to glycol cooling channels. Convective heat transfer will be the largest method of heat removal from the battery pack; h_c is the more commercially relevant parameter between the two.

The maximum temperature does increase significantly with the maximum specific energy compared to the base case (1044°C compared to 1027°C) because the base case of ~350 Wh/kg is already close to the maximum specific energy of ~400 Wh/kg for an LCO|LLZO|Li LiSSB if the minimum electrolyte thickness is 10μm and the minimum LLZTO volume fraction in the catholyte is 30%. The maximum temperature will change depending on the cathode material and electrolyte used, even

for the same specific energies used here, because the stoichiometric thermal decomposition of different layered metal oxide cathode materials generates different amounts of oxygen. In general, higher specific energy means more stored energy can be released to generate heat as well as lower thermal stability. So as the cathodes switch to higher specific energy materials such as high nickel content NMC cathodes, the expected maximum temperature should increase, and the onset temperature of thermal runaway should decrease.[59] Some electrolytes also contribute to thermal runaway by reaction with lithium which is another potential source of thermal management concerns.[16]

In the case of a 1:1 N:P ratio, lithium will be the limiting reactant for Li_2O formation oxygen evolved from the cathode, so it's unclear how much the total heat generated will increase if the electrolyte is also reactive. But in the case where lithium is in excess for Li_2O formation, the increase in total heat generated should be significantly higher with a reactive electrolyte than without. When changing the N:P ratio, we assume no change in volume in the total cell stack. In other words, for an N:P ratio > 1, the decrease in volume percentage occupied by the cathode is accompanied by increasing the volume percentage occupied by the cathode in the large format cell. We expect the maximum adiabatic temperature to reach a peak value at ~1.3 N:P ratio where the anode and cathode are balanced so that neither oxygen nor lithium is in excess for Li_2O formation. Unlike the adiabatic temperature rise, the observed temperature rise is dependent on more than the total amount of heat release, such as the rate of heat release and the rate of heat transferred to the environment. As the N:P ratio increases, the molar amount and surface area of lithium

increases which could also increase the reaction rate. It could be that the observed maximum temperature rise is at a higher N:P ratio than the expected maximum adiabatic temperature rise due to these factors.

κ is the most sensitive parameter in this model for both maximum temperature and maximum heating rate. When κ is 0.6, the maximum temperature is 1448°C and asymptotically approaches the adiabatic temperature of 1481°C for the large format cell. The maximum heat flow also increases by an order of magnitude to 245 W/g_{LCO}, however the total amount of heat produced remains the same. The only parameters we tested that change the total amount of heat produced are N:P ratio and specific energy. To reach close to the adiabatic temperature rise, the reaction between lithium and oxygen must be near instantaneous with no transport or kinetic limitations in the cell. If the reaction rate slows either by a lower κ value, or by decreasing the molar amounts of Li or O_2 available for reaction, then the maximum temperature and maximum heating rate will decrease significantly. When κ is set to $5x10^{-3}$, the maximum temperature decreases to 532°C which is only 197°C higher than the oven cutoff temperature. This corresponds to an order of magnitude decrease in the maximum heating rate to 0.26 W/g_{LCO}. The maximum temperature and maximum heat rate in the model with changing κ can be seen in **Figure 3.3**.

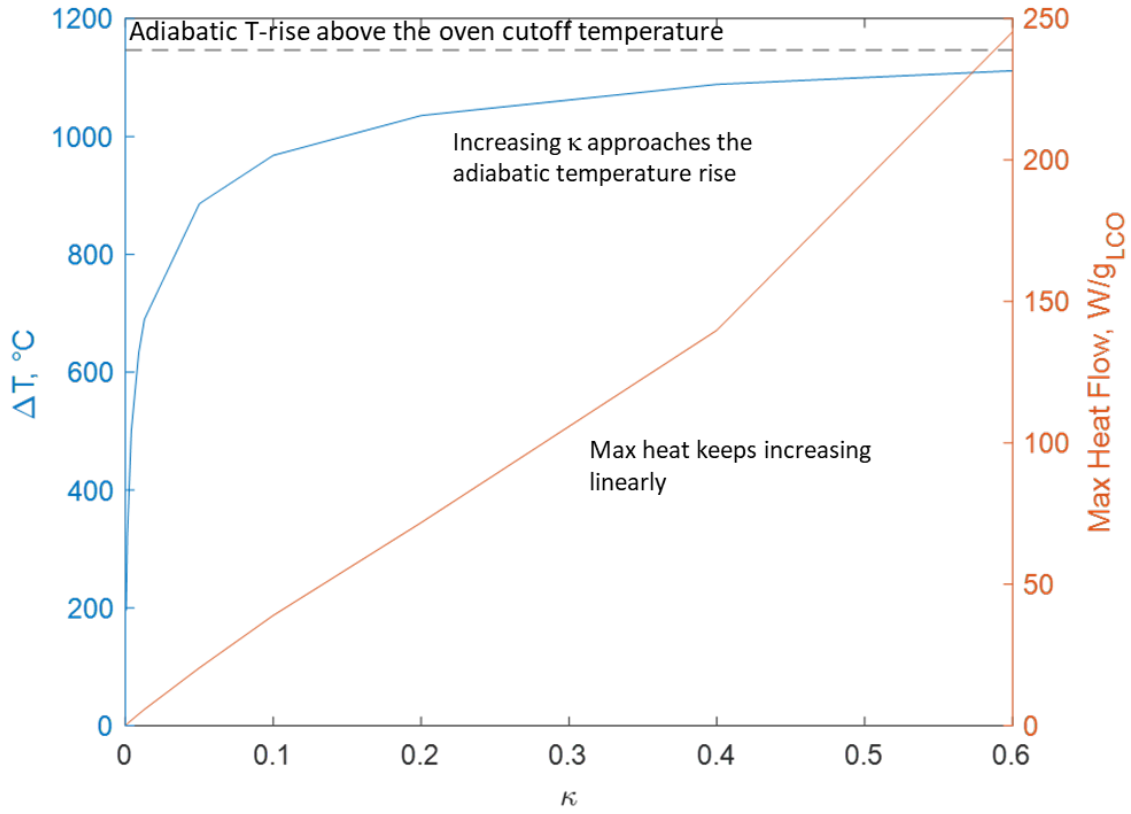

Figure 3.3. Maximum temperature rise above the oven cutoff temperature of 335°C and maximum heat flow vs. κ

Due to the logarithmic behavior of maximum temperature with respect to increasing κ, decreasing the rate of reaction does not have a significant impact on the maximum temperature until κ is reduced to less than 0.005. One potential method to achieve this is with a protective layer over the lithium that prevents or slows oxygen diffusion to the lithium. In theory, if the lithium metal anode were completely hermetically sealed from the cathode, then thermal runaway should not occur with an electrolyte such as LLZO that does not generate heat with either electrode. With more reactive electrodes such as sulfides and other ceramic oxides, the electrolyte itself can

be the source of self-heating when in contact with the electrodes.[16,60] Another method for reducing the maximum temperature and heating rate is by venting the O_2 before it has a chance to react with lithium. We do not consider any venting in this model.

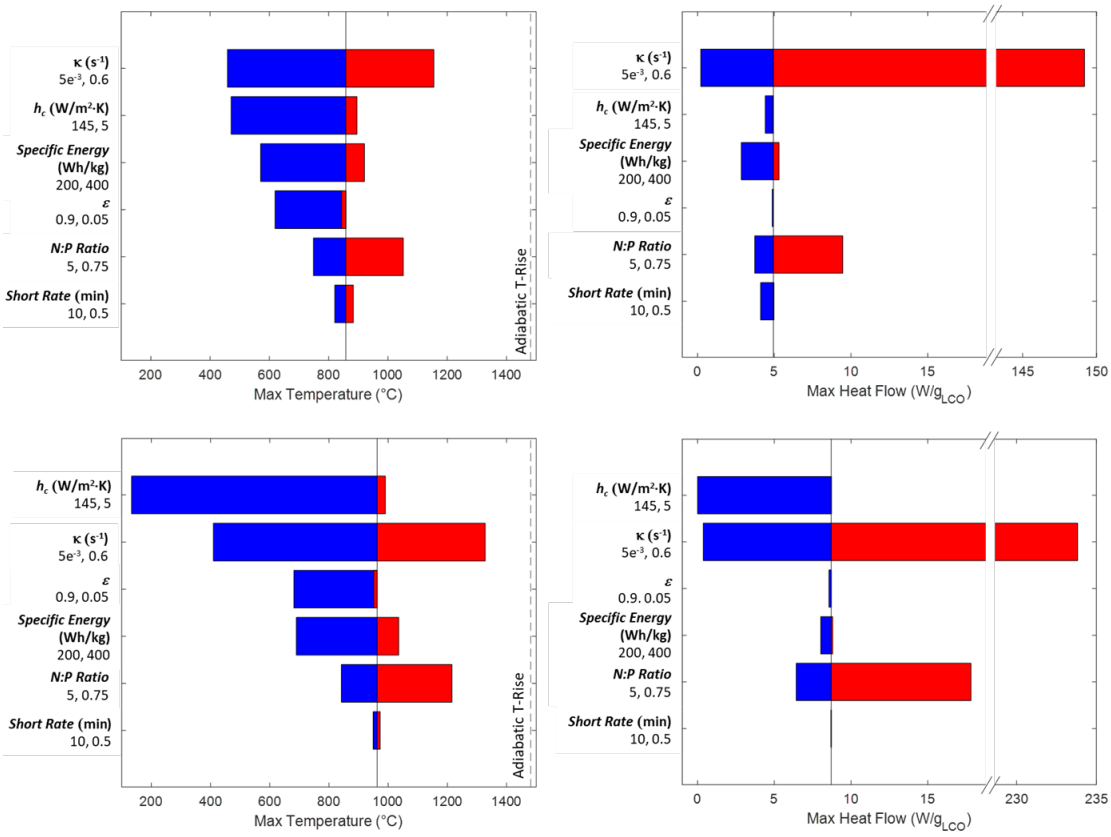

Figure 3.4. Short circuit tornado plots showing the variation in a) temperature at a point inside of the short circuit region, P_1 b) heat flow at P_1 c) temperature at a point outside of the short circuit region, P_2 d) heat flow at P_2. The two quantities underneath each parameter on the y-axis correspond to the low value and the high value for each parameter tested.

For the short circuit model, the base values at P_1 are a maximum temperature of 858°C and a maximum heating rate of 4.94 W/g_{LCO}, and the base values at P_2 are 963°C and 8.70 W/g_{LCO} (See Chapter 2 for the locations of P1 and P2 in the short circuit model). We swept the same parameters from the thermal ramp model through

the short circuit model with the addition of short circuit rate. κ is still the most sensitive variable for P_1 for increasing the maximum temperature but is nearly identical to h_c for lowering the maximum temperature. Convection is the most sensitive parameter for reducing the maximum temperature at P_2. P_2 is closer to the surface of the cell and if the convection is high enough it will prevent the outer portion of the cell from entering thermal runaway. In this model, the upper limit convective heat transfer coefficient is sufficient to prevent thermal runaway from spreading. Increasing convective heat transfer with a larger h_c does not prevent P_1 from entering thermal runaway due to the high rate of heat generation from the short circuit. Increasing κ increases the maximum temperature at both P_1 and P_2 more than any other parameter. P_2 has a larger reduction in maximum temperature for the lower value of κ compared to P_1 (553°C reduction in maximum temperature compared to a 399°C reduction in temperature) because the only source of internal self-heating at P_2 is Li_2O production while P_1 is also heated by the short circuit rate which is unaffected by the value of κ.

N:P ratio has the second highest impact on increasing temperature at both P_1 and P_2. N:P ratio sensitivity in this model is an important consideration because early iterations of commercialized LiSSBs will likely have an N:P ratio >1, thus making the thermal safety issue a greater concern. Similar to the thermal ramp, higher N:P ratios lead to higher temperatures due to the Li_2O equation formulation resulting in a faster rate of reaction as the Li content inside of the cell increases. κ incorporates transport limitations in our model as well, so as the N:P ratio increases, the lithium

surface area available for reaction also increases which would increase the rate of Li_2O production even if the kinetic rate of reaction is not changing. Further investigation into the reaction limitations of Li_2O formation is required. When sweeping specific energy, the maximum temperature does not increase much in the positive direction (~70°C increase at both P_1 and P_2 compared to the base values) but does decrease significantly at the lower specific energy (~280°C decrease at both P_1 and P_2 compared to the base values). This is more due to the difficulty in substantially increasing the specific energy of a LCO|LLZO|Li LiSSB. In order to increase the specific energy of a LiSSB much higher than 400 Wh/kg, a high energy density cathode such as high nickel content NMC cathode or reducing the mass of the electrolyte would be necessary. We also explore emissivity down to that of mylar (0.04), but in most single cell cases the emissivity will be higher (close to 1) as the cells can be painted black to increase the emissivity. This parameter is relevant for a thermal ramp test or nail penetration test, but the translation from these tests to battery pack behavior is not necessarily clear cut as little to no radiation should be present in a tightly packed battery back. The short rate has a surprisingly low sensitivity in the model. Part of this could be the location of the short on the edge of the cell. This location allows for higher heat transfer to the surroundings resulting in a suppressed maximum temperature at P_1. The temperature at P_2 also does not have much of a sensitivity to the short circuit, but this is likely due to the time scale of heat transfer from the shorted region to P_2. P_2 is far away from the short, so it takes longer to reach the thermal runaway onset temperature resulting in a relatively consistent maximum temperature despite the changing short rate. The sensitivity of short rate on

maximum temperature at P_2 will likely change if the short is spatially closer to P_2 or if the short region is larger.

Conclusions

In our model, k is by far the most sensitive parameter. According to this model, the best way to either mitigate or prevent thermal runaway is by either increasing transport limitations of oxygen to lithium or through some form of venting. The importance of the reaction between lithium and oxygen for thermal safety of LiSSB further reinforces the need for a more rigorous kinetic study of Li_2O formation, however this is very challenging due to the extremely exothermic nature of this reaction. Our model also shows that in the case of a short circuit, water/glycol mixtures in modern cooling systems could be sufficient to prevent thermal runaway from spreading to other cells, however water/glycol coolant systems typically are not designed to halt thermal runaway after it begins. These mixtures have very low boiling points (~110°C) potentially resulting in the boiling off of the coolant during thermal runaway. Our model also shows that is lithium foil is included in the assembly of an LiSSB (N:P capacity ratio > 1) then there is more heat that is generated and the maximum temperature increases. In this model, we did not consider reactions with cathode additives. Future work will include the cathode additives into our reaction system.

Chapter 4: 0D Model for LCO and NCA all-solid-state cells including cathode sheet additives

Introduction

We previously modeled a thermal ramp test and short circuit of a theoretical large format LiSSB using differential scanning calorimetry heat flow data for an "all-inclusive microcell."[15] We found that while the LiSSB thermal runaway onset temperature is significantly higher than Li-ion (250°C compared to ~150°C), the peak temperature and maximum heating rates are comparable. Our published work on this model only considered the exothermic formation of Li_2O and neglected the influence that the presence of conductive carbon, binder or gas venting could have on the thermal runaway behavior of a large format cell. However, our DSC work shown in Chapter 5 suggests that modeling only the formation of Li_2O formation and neglecting other cell components may not be sufficient to capture the thermal runaway behavior of our cell. In this work, we construct a 0D model that incorporates CO_2 evolution from oxygen reaction with conductive carbon as well as the pyrolysis of PVDF binder and subsequent reaction of HF with lithium into the thermal runaway reaction kinetics. We also model the higher energy density $LiNi_{0.8}Co_{0.15}Al_{0.05}O_2$ cathode without organic liquid electrolyte.

Modeling Methods

We model a 0D lumped model for a theoretical large format LCO| LLZO| Li all-solid-state lithium metal (LiSSB) as shown in **Figure 3.1**. We model two different large format chemistries: 1) 329 Wh kg^{-1} $Li_{0.47}CoO_2$ | LLZO | Li cell with a cathode

sheet consisting of 90 wt% active material, 5 wt% PVDF binder, and 5 wt% carbon, and 2) 419 Wh kg^{-1} $Li_{0.3}Ni_{0.8}Co_{0.15}Al_{0.05}O_2$ | LLZO | Li cell with a cathode sheet consisting of 90 wt% active material, 5 wt% PVDF binder, and 5 wt% carbon. In both cells, the cathode is at an equilibrium potential of ~4.2V, and the cathode and anode are capacity matched. Further details about the construction of these cells can be found in **Table 4.4**.

Equation (4.2.1) is the generalized Sestak-Berggren kinetic equation and was used to describe the kinetic rate of decomposition of the cathode material. **Table 4.1.** lists the parameters used in each of the cathode material variations. In the absence of solvent, little to no heat is released by the cathode, so we neglected any heat generation from the cathode material breakdown, and a single equation was sufficient to estimate the release rate of oxygen.[20,61] In the case of the highly exothermic decomposition of LCO and NCA in the presence of solvent, multiple equations would be needed to capture the more complex heat flow.[62]

$$\frac{dx_{P,i}}{dt} = -A_{P,i} e^{\frac{E_{P,i}}{RT}} x_{P,i}^{a,i} \left(1 - x_{P,i}\right)^{b,i} \quad (4.1)$$

Because the decomposition of layered metal oxides with more than one transition metal (such as NMC and NCA) can be a complicated multi-step process, we estimate the stoichiometric amount of oxygen release in NCA to follow that of $LiNiO_2$.[63–65]

Table 4.1. Parameters for equation (4.1)

Parameter	LCO Decomposition[20]	NCA Decomposition[62,66]
A_P	$3.78 \times 10^8\ s^{-1}$	$3.111 \times 10^{12}\ s^{-1}$
E_P	$1.14 \times 10^5\ J\ mol^{-1}$	$1.35088 \times 10^5\ J\ mol^{-1}$
a	1.62	1.2629
b	0	0.4056

Equation (4.2.2) is a stoichiometric balance for the rate of consumption of Li. The initial value of x_{Li} is governed by the lithiation state of the cathode. In the case of $Li_yNi_{0.8}Co_{0.15}Al_{0.05}O_2$, we use y=0.3, so the initial value of x_{Li} is set to 0.7. In the case of Li_yCoO_2, we use y=0.47, so the initial value of x_{Li} is set to 0.53.

$$\frac{dx_{Li}}{dt} = -2\frac{dx_{Li_2O}}{dt} - \frac{dx_{LiF}}{dt} - \frac{dx_{LiH}}{dt} \tag{4.2}$$

Equation (4.2.3) is a stoichiometric balance for the rates of production and consumption of oxygen. The rate of production of oxygen is set by the rate of decomposition of cathode shown in **Table 4.1.** and Equation (4.2.1). The rate of consumption of oxygen is the summation of the rates of formation of Li_2O and CO_2, as well as the rate of venting.

$$\frac{dx_{O_2}}{dt} = \sum v_{O_2}\frac{dx_{p,i}}{dt} - 0.5\frac{dx_{Li_2O}}{dt} - \frac{dx_{CO_2}}{dt} - \frac{dx_{O_2,vent}}{dt} \tag{4.3}$$

Equation (4.2.4) is the rate of production of Li_2O we used in our previous modeling publication.[13]

$$\frac{dx_{Li_2O}}{dt} = H(T)\kappa_{Li_2O}x_{Li}x_{O_2} \tag{4.4}$$

Equation (4.2.5) is the summation of the rate of formation of CO_2 and the rate of venting. The rate of formation of CO_2 is defined by power law kinetics and fit to DSC data.[67]

$$\frac{dx_{CO_2}}{dt} = \kappa_{CO_2} x_{O_2} P^n - \frac{dx_{CO_2,vent}}{dt} \tag{4.5}$$

Equation (4.2.6) is used to estimate the rate of breakdown of PVDF based on TGA mass loss during PVDF pyrolysis. Two equations are used to estimate this rate of pyrolysis and the parameters are summmarized in **Table 4.2.**[68] Note that these two equations are defined in terms of mass relative to the intial mass of PVDF in order to maintain conservation of mass, and we convert this value to moles per mole of active material for use in all other equations.

$$\frac{dy_{PVDF,i}}{dt} = A_{PVDF,i} e^{\frac{E_{PVDF,i}}{RT}} y_{PVDF,i}^{c_i} \tag{4.6}$$

Table 4.2. Parameters for equation (4.6)

Parameter	LCO Decomposition	NCA Decomposition
A_P	$6.0 \times 10^{30}\ s^{-1}$	$2.6 \times 10^{54}\ s^{-1}$
E_P	$4.66 \times 10^{5}\ J\ mol^{-1}$	$8.2 \times 10^{5}\ J\ mol^{-1}$
a	1	1
b	0	0

Equation (4.2.7) is the stoichiometric balance of HF production from the pyrolysis of PVDF with the consumption of HF through LiF and LiH formation as well as venting.

$$\frac{dx_{HF}}{dt} = \sum v_i \frac{dx_{PVDF,i}}{dt} - 0.5\frac{dx_{LiF}}{dt} - 0.5\frac{dx_{LiH}}{dt} - \frac{dx_{HF,vent}}{dt} \tag{4.7}$$

Equation (4.8) is the rate of formation of LiF and LiH based on the reaction system previously described.

$$\frac{dx_{LiF}}{dt} = \frac{dx_{LiH}}{dt} = -\kappa_{LiF} x_{HF} x_{Li} \tag{4.8}$$

We define the vent rate of each individual gas, *i*, by adapting a mass flow choking vent model published by Coman et. al. and shown in Equations 9-13.[69] The vent only turns on after a critical vent pressure of 34.5 bar is reached, and it remains open after bursting. Equation (4.9) defines the amount of gas that is ejected out of the cell via venting.

$$\frac{dx_{i,vent}}{dt} = \frac{P_{i,vent} V_{i,vent} A_{vent}}{x_i n_P R T_{vent}} \tag{4.9}$$

Equation (4.10) defines the pressure the vent is at when open as a function of the internal cell pressure and the Mach number.

$$P_{i,vent} = \frac{p_i}{\left(1 + \frac{\gamma - 1}{2} M^2\right)^{\frac{\gamma}{\gamma - 1}}} \tag{4.10}$$

Equation (4.11) defines the gas velocity through the open vent as a function of the temperature and Mach number.

$$V_{i,vent} = \sqrt{\frac{\gamma R T}{M_i}} M \tag{4.11}$$

Equation (4.12) defines the temperature of the vented gas.

$$T_{vent} = \frac{T}{1 + \frac{\gamma - 1}{2} M^2} \tag{4.12}$$

Equation (4.13) defines the Mach number for the two scenarios where the flow is either subsonic or choked. If the flow is choked, the Mach number is set to 1.

If the flow is subsonic, the Mach number is a function of the total internal cell pressure.

$$M = \begin{cases} \sqrt{\frac{2}{\gamma-1}\left(\left(\frac{P}{P_{amb}}\right)^{\frac{\gamma-1}{\gamma}} - 1\right)}, & P_{amb} > P\left(\frac{2}{\gamma-1}\right)^{\frac{\gamma}{\gamma-1}} \\ 1, & P_{amb} \leq P\left(\frac{2}{\gamma-1}\right)^{\frac{\gamma}{\gamma-1}} \end{cases} \quad (4.13)$$

Equation (4.14) defines the rate of temperature change in the cell from the summation of heat transfer to the environment from convection, internal heat generation from chemical reaction, and cooling due to gas venting. We leave emissivity out Equation (4.14) because emissivity should be 0 in a tightly packed battery pack.

$$\frac{dT}{dt} = \frac{(T_{ext} - T)h_c S + \sum Q_i}{C_p m} + \sum \frac{dx_{i,vent}}{dt}\frac{m_p T}{m} \quad (4.14)$$

T_{ext} is a linearly ramping temperature starting at 25°C and increasing at a rate of 5°C min^{-1} until a cutoff temperature of 335°C is reach. For the remainder of the test, the oven will maintain at 335°C. Q_i is the heat generation from exothermic and endothermic events such as lithium metling, Li_2O formation, etc. The general equation for Q_i can be seen in Equation (4.15), and the parameters are listed in **Table 4.4.**

$$Q_i = \Delta H_i \frac{dx_i}{dt} n_P \quad (4.15)$$

Results and Discussion

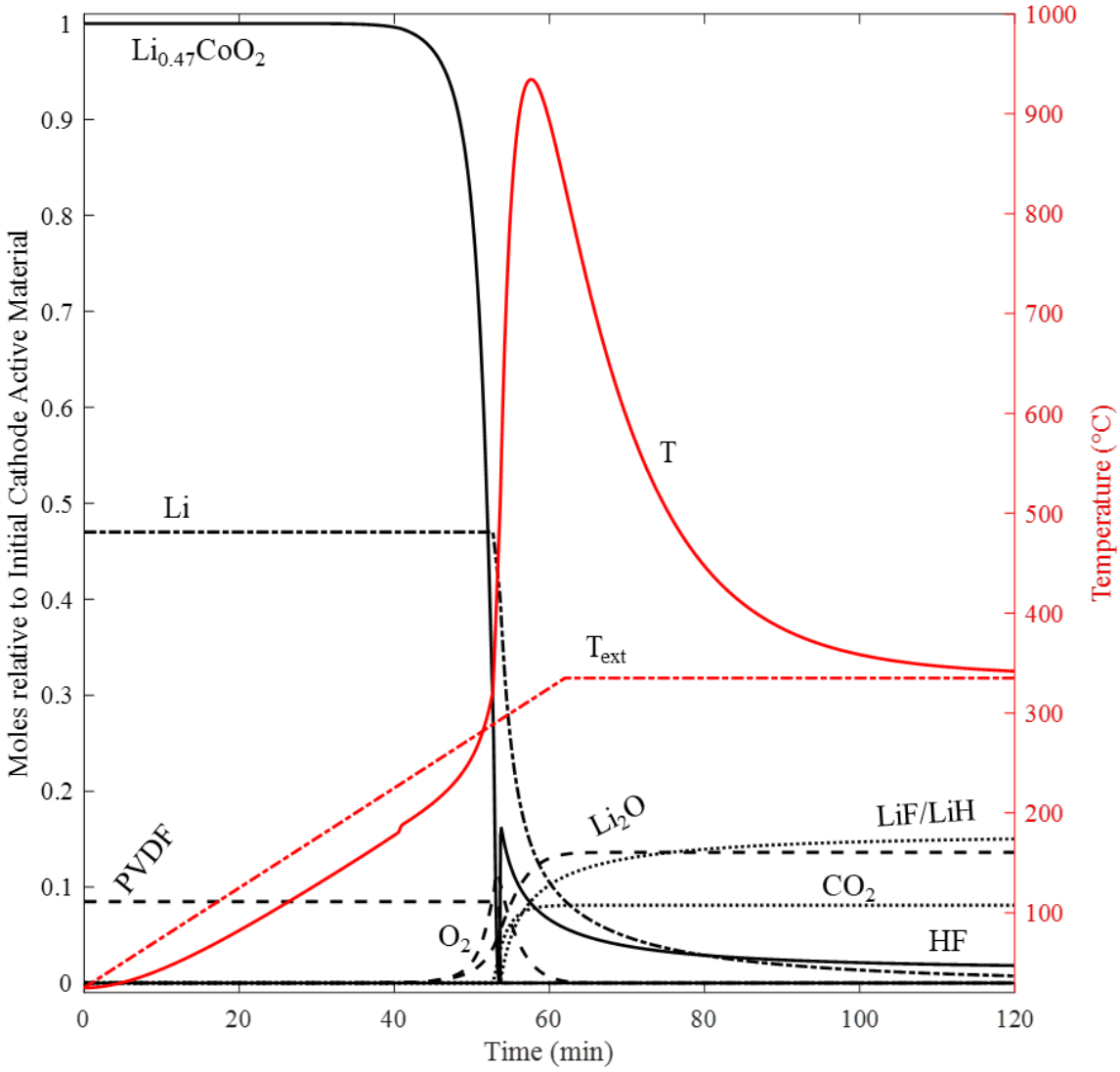

Figure 4.1 Temperature and molar amount of all reactants/products present in an LCO|LLZO|Li large format cell without venting.

Figure 4.1. shows the thermal runaway behavior of an $Li_{0.47}CoO_2$|LLZO|Li cell in the absence of any venting. When the cell temperature reaches ~200°C, $Li_{0.47}CoO_2$ decomposition begins resulting in the release of oxygen. There is an initial

formation of a Li_2O crust protecting pristine lithium from further reaction. The development of higher pressures in the cell causes faster CO_2 formation kinetics which corresponds to a higher order power law as seen in Equation (4.5). The reaction enthalpy for Li_2O formation is over 3x higher per mole of oxygen gas than the reaction enthalpy of CO_2 (1213 kJ mol^{-1} compared to 389 kJ mol^{-1}). The presence of conductive carbon causes a reduction in the total amount of heat generated than in a case without conductive carbon, however this is still exothermic enough to cause thermal runaway. With the inclusion of conductive carbon, exothermic reaction begins self-heating in the cell the moment oxygen begins to release from the cathode. This compares to a ~70°C delay between oxygen release and the self-heating onset temperature from the model without conductive carbon present. After thermal runaway is triggered, the pyrolysis of PVDF occurs within 30 seconds and completely decomposes in under 1 minute. This rapidly releases HF into the cell which then begins to react with lithium alongside oxygen. LiH and LiF are formed at the same rate in this model. Note that lithium is left over at the end of this test as we do not factor in any lithium uptake by the LLZO electrolyte.[25] Ultimately, thermal runaway lasts a total of 6 minutes from the beginning of thermal runaway until the peak temperature is reached and the cell begins to cool back down with a maximum heating rate of 323°C min^{-1}. The model shown in chapter 2 has a total time of thermal runaway of ~10 minutes which is slightly longer without the carbon and PVDF present. The total amount of heat released was reduced with a total temperature rise of 599°C above the oven temperature compared to 705°C in the model from chapter 2.

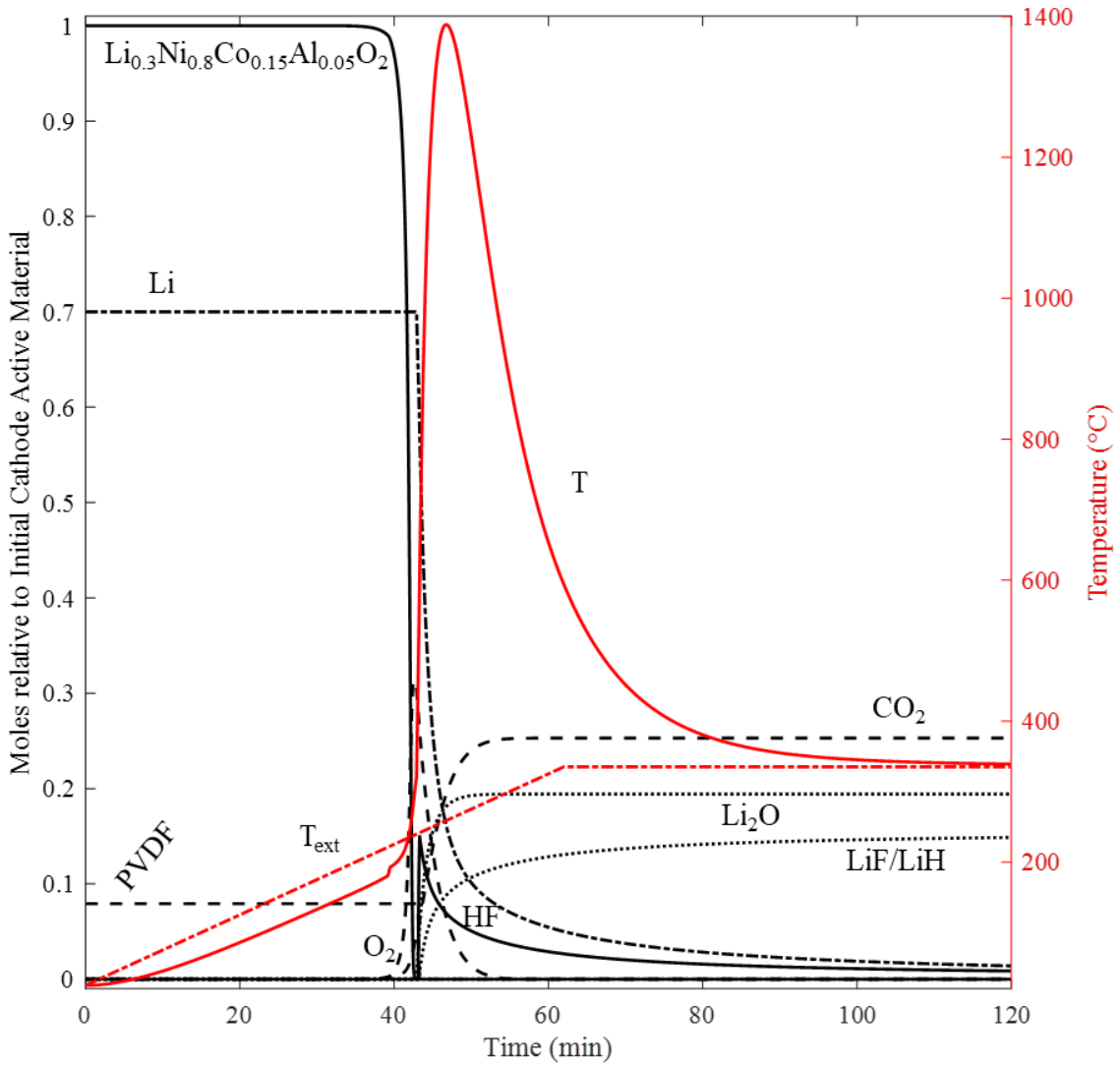

Figure 4.2 Temperature and molar amount of all reactants/products present in an NCA|LLZO|Li large format cell without venting.

Figure 4.2. shows the thermal runaway behavior of an NCA|LLZO|Li cell in the absence of any venting. In the case of LCO with no solvent present, the Co transition metal will only reduce to Co^{2+}/Co^{3+} present in Co_3O_4 in the temperature range that we test, but the Ni will reduce entirely to Ni^{2+} seen in NiO. This results in greater oxygen loss from high nickel-content cathode materials than high cobalt

content even in comparable lithiation states in all-solid-state cathodes. This results in greater heat generation during thermal runaway as there is more oxygen present for CO_2 and Li_2O formation as well as less lithium remaining after the test is done. In our model, we see a maximum temperature rise of 1053°C which is 454°C greater temperature rise than what is seen in the LCO model. The total time of reaction is shorter compared to the LCO model at ~3 minutes with a maximum heating rate of 772°C min^{-1}. About 30 seconds after thermal runaway begins, PVDF breaks down and releases HF. At the end of thermal runaway, ~25% of the initial lithium present remains despite the increased oxygen release from the high Ni cathode because of the CO_2 reaction, however we do slightly overestimate the amount of oxygen generated in this model as we treat NCA like $LiNiO_2$.

In both cases without venting, pressures on the order of 1000s of bar are achieved assuming a headspace volume of 10% of the total cell stack volume. These pressures are not realistic for a commercialized cell as no cell casing will be capable of withstanding those pressures. Realistically, the maximum temperatures shown in a cell without venting will likely not be observed. As most of the major heat generating reactions are driven by gas-solid reactions, a vent could theoretically remove the gaseous reactant before it has a chance to generate a significant amount of heat. As an added benefit, venting gas allows for some cooling of the cell due to heat transfer with the flowing gas.

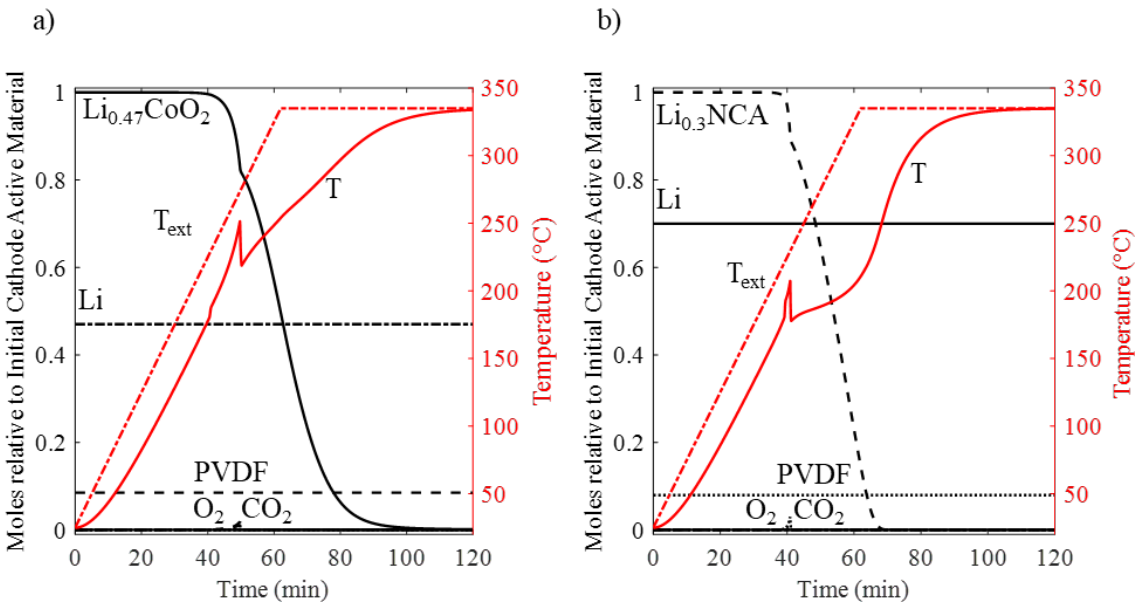

Figure 4.3. a) LCO|LLZO|Li cell results and with venting at 34.5 bar and an oven cutoff temperature at 335°C b) NCA|LLZO|Li cell results with venting at 34.5 bar.

Figure 4.3. panel a) shows the results of the solid-state $Li_{0.47}CoO_2$|LLZO|Li cell model, but with a choked mass flow venting model. When the headspace pressure reaches 34.5 bar (the burst pressure of an 18650 cell), the vent cap pops, and gas flows out and cools the cell with it. Oxygen does begin to form CO_2 before it is vented, so some slight exothermic heat generation does occur resulting in some self-heating. When the vent pops at ~50 minutes, the temperature in the cell immediately decreases by ~ 30°C at a rate ~150°C min^{-1}. The same can be seen in the solid-state $Li_{0.3}Ni_{0.8}Co_{0.15}Al_{0.05}O_2$|LLZO|Li model in panel b) except the point at which the vent bursts is at a lower temperature due to the lower thermal stability of $Li_{0.3}Ni_{0.8}Co_{0.15}Al_{0.05}O_2$ compared to $Li_{0.47}CoO_2$. The all-solid-state NCA cell also begins to enter thermal runaway due to rapid oxygen released and CO_2 formation, but the vent cools off the cell and removes oxygen preventing thermal runaway from

progressing. In both cases, thermal runaway was stopped in our model because the oxygen was vented from the cell which cooled the cell, and nothing remained behind to react with the lithium cathode. When the oven cutoff temperature was set to 335°C, the cell did not self-heat to a high enough temperature to pyrolyze PVDF and instead equilibrated at the ambient external temperature.

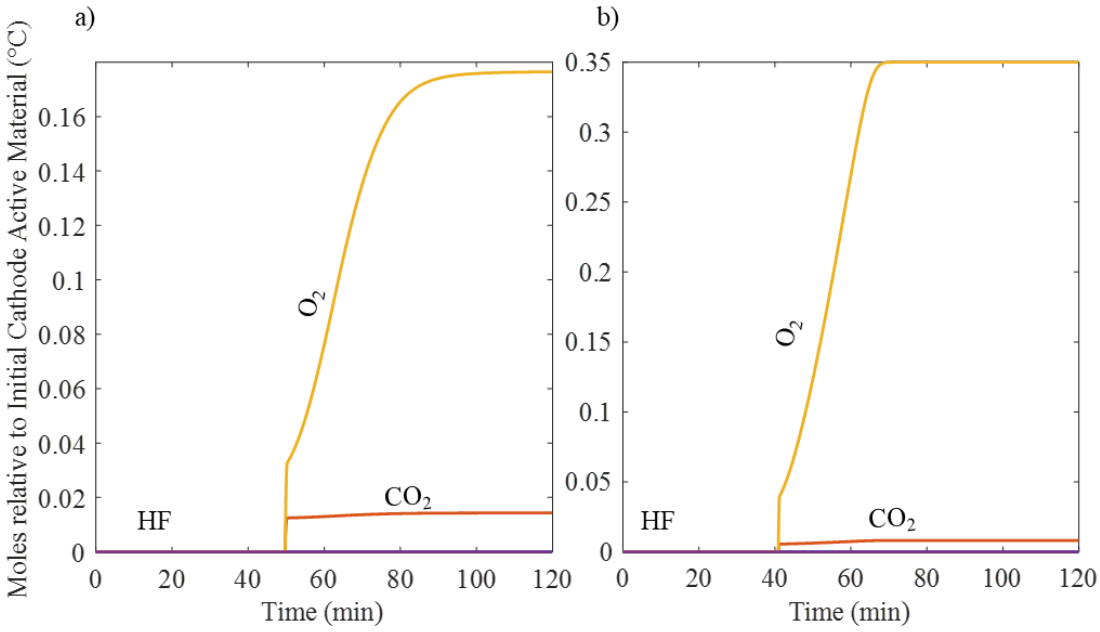

Figure 4.4. Composition of gases being vented at a venting pressure of 34.5 bar in a) LCO|LLZO|Li cell results and b) NCA|LLZO|Li cell results.

The main gas that will be ejected will be pure oxygen as seen in **Figure 4.4**. Some oxygen does react to form CO_2 prior to venting, and this trend continues even after the vent bursts, but the majority of the gas ejected is oxygen at >200°C. This could introduce a further safety hazard for the battery pack as a whole if the ejected oxygen were to react during venting. Not only does the amount of oxygen vented increase with the less thermally stable $Li_{0.3}Ni_{0.8}Co_{0.15}Al_{0.05}O_2$ because the Ni reduces to NiO, but oxygen evolves at a faster rate than $Li_{0.47}CoO_2$ resulting in a shorter

residence time for CO_2 formation before the cell vents. In both of these cases, the oven is set to a lower temperature than the onset temperature of PVDF pyrolysis which results in no HF evolution, and no HF ejection. In a case where a cell is heated beyond the pyrolysis temperature of PVDF, HF would also be vented along with pure oxygen.

Figure 4.5. shows the same oven test, but with a vent pressure of 3 bar to match that of the burst pressure of a pouch cell. Because the cells bursts and venting starts within a few minutes of the cathode material first evolving oxygen, the initial cooling from the vent is much smaller only cooling the cell by 1°C in the LCO cell and by 5°C in the NCA cell, however continued cooling does occur as more oxygen is vented.

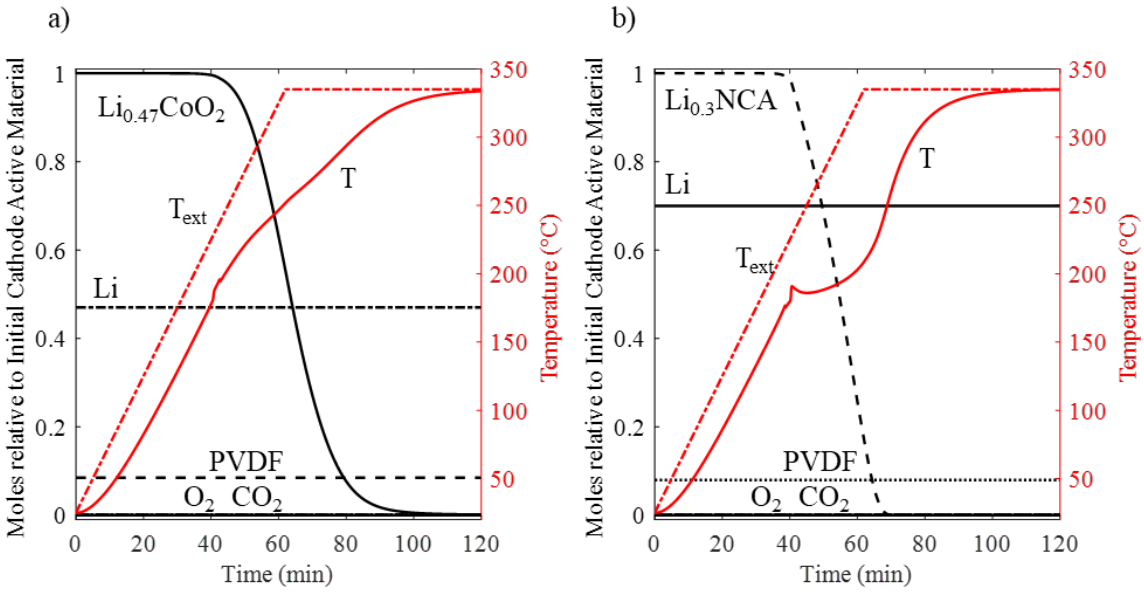

Figure 4.5. a) LCO|LLZO|Li cell results with venting b) NCA|LLZO|Li cell results with venting at 3 bar. Oxygen and carbon dioxide can vent as soon as they are evolved right after the vent bursts.

Figure 4.6. shows the total amount of each gas that is vented during the test. Only about 0.003 moles of CO_2 per mol of active material gets vented in both the NCA and LCO cells because oxygen is vented out of the cell before it has a chance to react. This limits the heat generation within the cell, but this also means that the ejected gas is almost entirely pure oxygen at a temperature >200°C. In both cells, not enough heat generation occurs to reach the PVDF pyrolysis temperature, so no HF is generated or vented.

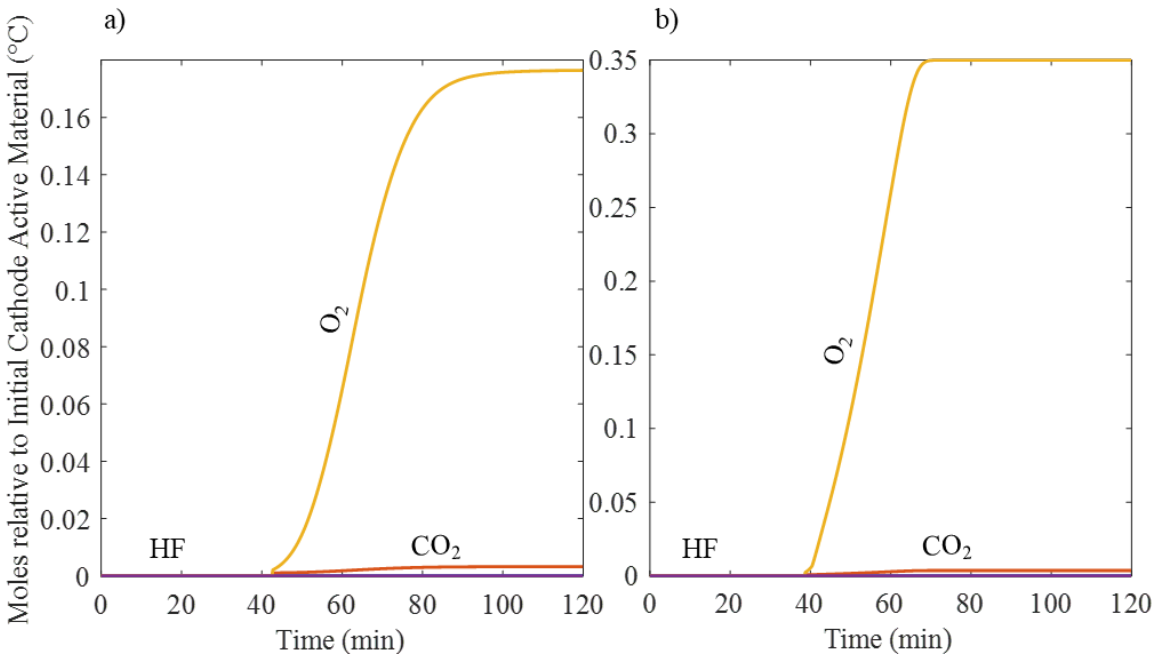

Figure 4.6. Composition of gases being vented at a critical pressure of 3 bar in a) LCO|LLZO|Li cell results with venting and b) NCA|LLZO|Li cell results. In both cells, the ejected gas is almost entirely comprised of O_2, and no HF is generated.

Conclusions

The inclusion of reactions involving the PVDF binder and conductive carbon in the cathode is an important addition to better model the thermal runaway behavior

of a large format cell. By including reaction of oxygen with the conductive carbon, the onset temperature of self-heating is reduced by ~70°C in the $Li_{0.47}CoO_2$ model, and the maximum rate of temperature rise of 323°C min^{-1} when no venting is included which is ~75°C min^{-1} faster than the maximum rate of temperature rise without including HF and carbon reactions. Modeling the higher energy density NCA resulted in even greater maximum temperatures with a temperature rise of 1053°C above the oven temperature, and a maximum heating rate of 772°C min^{-1}. However, in order to achieve these temperatures, no venting can occur which generates non-physical pressures >1000 bar. When venting at 34.5 bar is included, thermal runaway is stopped entirely in both the $Li_{0.47}CoO_2$ and $Li_{0.3}Ni_{0.8}Co_{0.15}Al_{0.05}O_2$ cells, and the majority of the initial self-heating prior to venting comes from CO_2 formation resulting in almost no lithium reacting during the course of heating. Venting could be a viable solution to prevent thermal runaway entirely in all-solid-state cells, however the composition of the ejected gas will be >90% pure oxygen with the partial pressure of CO_2 decreasing as the burst pressure of the vent also decreases which could result in potential safety hazards if the oxygen reacts as it's vented.

Model Parameters

Table 4.3. Table of symbols

Symbol	Definition
T	Cell temperature
R	Ideal gas constant
$A_{i,j}$	Kinetic frequency factor of reaction *j* for species *i*
$E_{i,j}$	Activation energy of reaction *j* for species *i*
x_i	Molar ratio of species *i* relative to the initial moles of cathode active material
P	Total pressure
p_i	Partial pressure of species *i*
$y_{PVDF,i}$	Mass ratio of PVDF reactant in reaction *i* relative to initial mass of PVDF
υ_i	Stoichiometric coefficient of species *i*
κ_i	Kinetic and transport limitation coefficient for the formation of species *i*
P_{vent}	Vent pressure
V_{vent}	Vent velocity
A_{vent}	Vent area
n_P	Initial moles of cathode active material
T_{vent}	Vent Temperature
γ	Constant pressure to constant volume heat capacity ratio
M	Mach number
M_i	Molar mass of species *i*
P_{amb}	Ambient pressure outside of the cell
T_{ext}	External oven temperature
$C_{p,i}$	Specific constant pressure heat capacity of species *i*
h_c	Heat transfer coefficient
Q	Heat from reaction and phase change
$H(i)$	Heaviside function dependent on variable i
$x_{i,vent}$	Amount of species *i* ejected from the vent relative to initial moles of cathode active material
m_p	Mass of the cathode active material
m	Total cell mass
ΔH_i	Enthalpy of reaction for the formation of species *i*

Table 4.4. Table of cell properties

Parameter	Value	Reference/Notes
Cathode thickness	80 μm	
N:P Ratio	1	
Electrolyte thickness	10 μm	
Al and Cu Thicknesses	5 μm	
Cathode Active Volume Fraction	0.70	
Cathode volume fraction of LLZO	0.20	
Active Material Loading	90 wt%	
PVDF Loading	5 wt%	
Carbon Loading	5 wt%	
$C_{p,average}$	0.84 $\frac{J}{g \cdot K}$	See Chapter 2
h_c	3.56× 10^{-3} $\frac{W}{cm^2 K}$	
Specific Energy for LCO Cell	329 $\frac{Wh}{kg\ cell\ repeat\ layers}$	For a 3.9V average discharge voltage starting from $Li_{0.47}CoO_2$
Specific Energy for NCA Cell	419 $\frac{Wh}{kg\ cell\ sandwich}$	For a 3.7V average discharge voltage starting from $Li_{0.47}CoO_2$
κ_{Li_2O}	0.0129	[13]
T_{react}	330°C	
$\Delta H_{Li\ melt}$	432.21 $\frac{J}{g\ Li}$	
ΔH_{Li_2O}	-607 $\frac{kJ}{mol\ Li_2O}$	Corrected for 300°C
$\Delta H_{LiF+LiH}$	-464.2 $\frac{kJ}{mol\ LiF\ or\ LiH}$	Corrected for 400°C
ΔH_{CO_2}	-389 $\frac{J}{mol\ CO_2}$	Corrected for 300°C
n_P for LCO cell	10.39 mol	
n_{Li} for LCO cell	5.51 mol	
n_P for NCA cell	9.38 mol	
n_{Li} for LCO cell	6.57 mol	
m for LCO cell	1.75 kg	
m for NCA cell	1.56 kg	
γ	1.4	

Chapter 5: Differential Scanning Calorimetry Measurements of Lithium Metal Solid State Batteries to Determine Reaction Thermochemistry and Assess Thermal Runaway Safety

Introduction

Inoue and Mukai provide a key work quantifying heat release by building an "all-inclusive microcell" by placing an anode, separator, and charged cathode active material inside of a differential scanning calorimetry (DSC) pan and heating it at 5°C/min. However, they used 1mg pressed LCO pellets delithiated to $Li_{0.47}CoO_2$ and 1mg of lithium metal resulting in an N:P capacity ratio of ~20:1; an ideal commercial LiSSB should have a 1:1 N:P ratio, so it would be constructed with no lithium in the anode initially.[15] The only reaction observed in the Inoue and Mukai work is the formation of Li_2O as no conductive carbon, binder, or current collectors were included, and at the N:P ratio used, lithium is in excess. For a 1:1 N:P ratio with an LCO cathode, lithium is limiting for Li_2O formation. Many commercial cathodes use a fluorinated binder such as poly(vinylidene fluoride) (PVDF) which results in HF generation upon heating, as well as conductive carbon which can react with O_2 and change the DSC heat flow results.[47,62,70] Accurate DSC microcell data can be used to predict thermal safety of a large format cell through modeling without performing an expensive and dangerous test on a large format cell in the early materials-level stages of battery development, although direct experimental testing of commercial cells is

still required.[13] There are some limits to using DSC data to construct a large format thermal runaway model, including (1) the large format models predict uncontrolled thermal runaway behavior causing temperature rise rate of ~250°C/min from a controlled temperature ramp experiment at ~5°C/min, (2) there could be discrepancy in the transport limitations on a ~1mg sample of lithium compared to a 30 cm x 10 cm Li anode, and (3) the kinetics of reaction in a high pressure hermetically sealed DSC pan where O_2 partial pressures can reach ~40 bar is different than in a vented commercial battery casing. However, the total amount of specific heat generated in a carefully balanced microcell should reflect that of a large format cell assuming no materials escape from the cell.

In this work, we perform DSC heat flow analysis on "all-inclusive microcells" with an LCO cathode, lithium metal anode, and a $Li_{6.4}La_3Zr_{1.4}Ta_{0.6}O_{12}$ (LLZTO) electrolyte. The LLZTO was kept in excess to prevent contact between the lithium metal and cathode sheet, but because LLZTO does not participate in any reaction with a significant enthalpy this should not increase our heat flow at all.[16] In other words, it is most important to get the correct ratios among reactive cell components, which for the present study is primarily the Li metal and the cathode sheet. We use LCO cathode sheets with 5 wt% Super P conductive carbon and 5 wt% PVDF binder with a nearly capacity matched lithium metal anode. Including these extra cathode components is an important delineation between our work and the work by Inoue and Mukai as the fluorinated binder and conductive carbon will likely be present in a commercialized large-format cell, and they do not remain inert during DSC experiments or during thermal runaway. The present work focuses only on a

$Li_{0.43}CoO_2$ cathode sheet. We also build our microcells at about a 1:1 N:P ratio as lithium will be the limiting reactant. In other words, for a $Li_{0.43}CoO_2$ cathode and a 1:1 N:P capacity ratio, O_2 is stoichiometrically in excess for the formation of Li_2O and all lithium in the anode should be consumed. This may lead to extra measured heat than what would be seen in a commercialized cell as there would be more lithium around to react with oxygen as well as other evolved gases in the cell such as CO_2 and HF. Performing DSC heat flow testing on a carefully assembled microcell in correct material ratios can be an important method to assess thermal safety on the materials level early in the cell development process. In summary, the contribution of this work is to provide a quantified thermochemistry map for a $Li_{0.43}CoO_2$ | LLZTO | Li LiSSB materials set, by matching known reaction enthalpies with DSC heat flow data, using carefully constructed microcells with commercially available materials and capacity-matched electrodes.

Methods

Materials

Cathode sheets consisting of 90 wt% LCO, 5 wt% Super P conductive carbon, and 5 wt% PVDF binder on 16mm aluminum current collectors were purchased from NEI corporation. The areal capacity of the cathode sheet is 2.0 mAh/cm^2 for a charged lithiation state of $Li_{0.43}CoO_2$ which corresponds to a maximum cutoff voltage of 4.3V. 0.7mm thick LLZTO electrolyte pellets manufactured by Ampcera were

purchased from MSE Supply. Lithium ingots with a purity greater than 99.9% were purchased from Sigma-Aldrich.

Cathode Preparation and TGA Analysis

Lithium half-cells were prepared in a 20mm split coin cell with 1M $LiPF_6$ in ethylene carbonate/dimethyl carbonate and a polypropylene/polyethylene Celgard trilayer separator. The cathode sheets were delithiated at a rate of C/10 and held at a constant voltage of 4.3V until the current dropped below C/100. We define fully charged cathode sheets as having a voltage of 4.3V vs. Li/Li^+, which corresponds to $Li_{0.43}CoO_2$. The cathode sheets were removed from the split coin cell after delithiation, washed with diethyl carbonate solvent more than 10 times, and dried overnight in a vacuum oven at 70°C. TGA of the LCO cathode sheet was performed on a TA Instruments SDT650 in an alumina crucible at 2°C/min to match the ramp rate of the DSC test.

Microcell Construction and DSC Testing

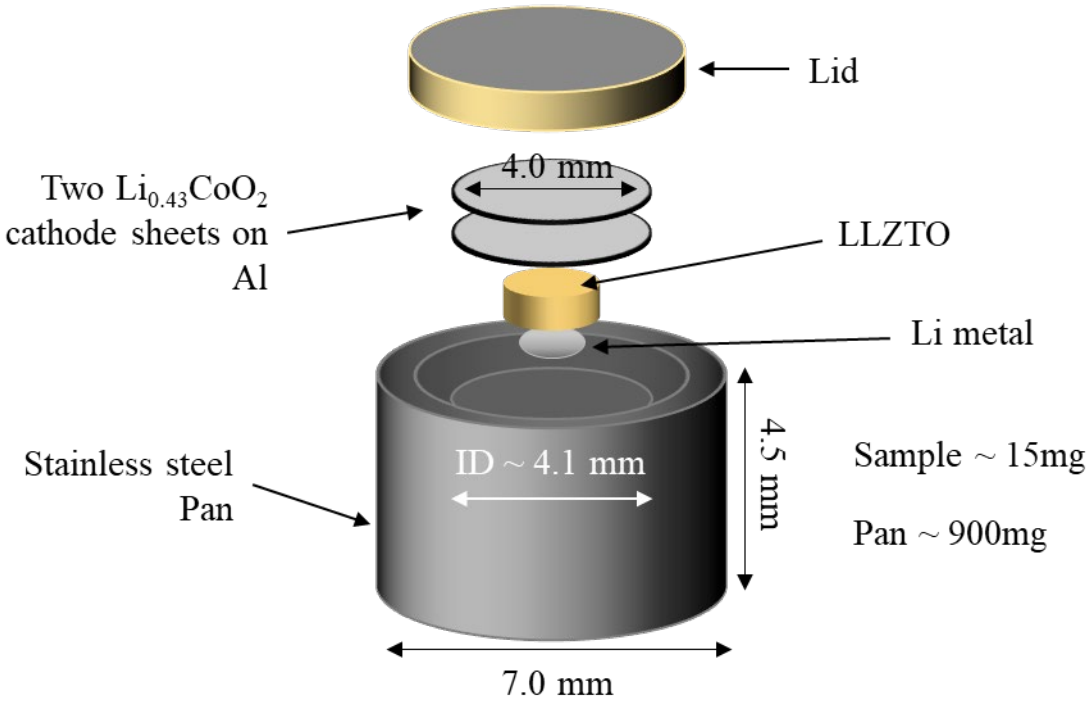

Figure 5.1. To-scale schematic of microcell built in a hermetically sealed stainless steel DSC pan. The electrodes are capacity matched and the electrolyte has a large enough surface area to cover the lithium metal anode entirely to prevent contact between the anode and the cathode.

All work with battery materials and microcell preparation was carried out in an Ar-filled MBraun glove box. Cathode sheets were cut into 4mm circles (~0.25 mAh per cutout) with a punch. We used two cutouts per microcell for a total of ~4.6mg of total charged cathode sheet (~0.50 mAh) including the aluminum current collectors. Lithium ingots were stored in light mineral oil to prevent reaction with the glovebox environment over time. We cut Lithium samples with a razor blade carefully to prevent mineral oil contamination on the sample and weighed to ~136 ± 2 µg (~0.50 mAh).. We made sure the sample cut was from the center of the ingot where lithium should be at the manufacturer's listed purity. The LLZTO pellets were

fractured to pieces with a mass between 8mg and 12mg. To assemble the microcell, which is where the lithium, LLZTO, and cathode sheet are all present in the DSC pan, the lithium layer was pressed on the bottom of the pan to ensure adequate thermal contact between the sample and the pan; no copper was included in the DSC pan for this reason. The LLZTO separator was placed over the lithium and pressed into the lithium to ensure spatial separation between the two electrodes so no reaction from direct contact of lithium with the cathode sheet could occur. The cathode sheets were placed in the pan last. We are limited by the minimum mass of lithium that we can accurately measure, so we use two cathode sheets rather than one to increase the accuracy of measuring the Li mass and thereby ensure the electrodes in the microcell are capacity matched. The microcell was hermetically sealed in a 20 μL high-pressure stainless-steel pan that weighs ~910mg. The hermetic sealing is a key point as we have no gas venting in our microcell resulting in partial pressures of oxygen potentially climbing to over 40 bar in our 20 μL pan assuming none of the oxygen reacts and our microcell materials occupy ~4 μL of the pan volume. We used a 2°C/min ramp rate in the temperature range of 40°C to 500°C on a TA Instruments Discovery DSC25 to ensure temperature gradients within the sample were kept to a minimum despite the large sample and pan mass (~15mg sample in a ~910mg pan). We did not pre-melt the lithium to ensure lithium did not react with anything in the pan prior to the test because we observed $Li_{0.43}CoO_2$ decomposition beginning at temperatures lower than the lithium melting point. After the initial run finished, we first cooled and then ran the microcell again at 2°C/min between the temperature range of 175°C and 190°C. The post-test enthalpy of lithium melting was compared

to the initial lithium melting enthalpy to estimate how much lithium reacted during the run.

Integration and Analysis

Due to the large mass of our pans (~910mg), thermal gradients have the potential to develop throughout the sample pan. We started our testing at 4°C/min but lowered the ramp rate to 2°C/min to minimize these potential thermal gradients, as they can contribute to baseline drift. However, some baseline drift could be observed even when an empty pan was used as the sample. To integrate the resulting heat flow curves, we fit the empty sample pan heat flow with a polynomial to serve as a heat flow baseline. Due to the high-pressure rating of the hermetically sealed DSC pan and its method of sealing, we are unable to reopen the pan after testing. Therefore, we cannot perform any materials characterization test on the sample after testing. We instead opt for an approach where we use the known enthalpies of reactions that we expect for the materials in the pan and align them with the DSC data. We adjust the enthalpies of reaction for elevated temperature by using tabulated temperature-dependent heat capacity data for the reactants and products in each reaction. We also assess the Gibbs free energy of each reaction to ensure that they are thermodynamically spontaneous in the temperature ranges we expect them to occur.

Results and Discussion

Reaction pathways during DSC experiments

Below we have listed a possible set of reactions that would occur during our DSC testing for a $Li_{0.43}CoO_2$ | LLZTO | LCO cell. We have divided the reactions taking place into 4 distinct peaks and temperature regions. Peak I (shown in **Figure 5.2** a, b, h) is the melting point of lithium which is an endothermic peak that occurs at ~180°C. Region II (shown in **Figure 5.2** f, g) is between 170°C and 250°C where exothermic heat flow is mainly from $Li_{0.43}CoO_2$ decomposition (reactions 2.1 and 2.2) . Region III (shown in **Figure 5.2** f, g) is between 250°C and 400°C and comprises of reactions caused by oxygen released in reactions (2.1) and (2.2) and then present in the microcell (reactions 2.3 – 2.5). Region IV (shown in **Figure 5.2**b, c, e, f, g, h) is between 400°C and 500°C and comprises of reactions caused by the breakdown of PVDF and subsequent HF formation (reactions 2.6 – 8). All enthalpy values have been adjusted for temperature (i.e., the enthalpy of reaction values are reported at standard conditions, and we correct the values based on the heat capacities of the species in the reaction and the temperature of the reaction) and are for a cathode sheet that is 90 wt% $LiCOO_2$, 5 wt% PVDF, and 5 wt% Super P.

Table 5.1. Microcell thermochemical reaction system with temperature adjusted enthalpies of reaction

Reaction #	Reaction	Temperature adjusted enthalpy
(5.1)	$Li_xCoO_2 \rightarrow xLiCo_2O_2 + \frac{1-2x}{3}Co_3O_4 + \frac{1-2x}{3}O_2$	$\Delta H_1 = -0.94\, J/mAh$
(5.2)	$LiCo_2O_4 \rightarrow Li_2CoO_2 + \frac{1}{3}Co_3O_4 + \frac{1}{3}O_2$	$\Delta H_2 = 0.40\, J/mAh$
(5.3)	$O_2(g) + 4Li(l) \rightarrow 2Li_2O(s)$	$\Delta H_3 = -14.71\, J/mAh$
(5.4)	$O_2(g) + C(s) \rightarrow CO_2(g)$	$\Delta H_4 = -4.74\, J/mAh$
(5.5)	$Li_2O + CO_2 \rightarrow Li_2CO_3$	$\Delta H_5 = -1.79\, J/mAh$
(5.6)	$[-C_2H_2F_2-]_n \rightarrow 2nC + 2nHF + H_2$	$\Delta H_6 = -0.97\, J/mAh$
(5.7)	$Li_2CO_3 + 2HF \rightarrow 2LiF + CO_2 + H_2O$	$\Delta H_7 = -0.91\, J/mAh$
(5.8)	$2Li + HF \rightarrow LiF + LiH$	$\Delta H_8 = -5.03\, J/mAh$

Reaction (5.1) is the conversion of Li_xCoO_2 layered metal oxide to an unstable intermediate $LiCo_2O_4$ spinel. Reaction 5.2 is the decomposition of the unstable intermediate spinel to form a stable Co_3O_4 spinel with further oxygen release.[63] Reaction 5.3 is the formation of Li_2O from evolved oxygen and the lithium metal anode. This is a highly exothermic reaction, but it should be more self-limiting for lithium with a higher surface area to volume ratio (e.g. a spray of lithium droplets will have less transport limitations than an ingot of lithium) prior to 300°C as it occurs on the surface of lithium and forms a crust-like layer on lithium.[39] Reaction 5.4 is the reaction of oxygen gas with Super P in the cathode sheet. Reaction 5.5 is the reaction between evolved carbon dioxide from reaction 5.4 and the Li_2O surface layer from reaction 2.3 forming a dense and stable surface layer of Li_2CO_3. This

reaction only occurs to a small degree with previous studies showing only a 6 wt% increase from reaction after chemical sorption of CO_2 on Li_2O up to >500°C.[71] Reaction 5.6 is the pyrolysis of PVDF. This reaction may involve multiple steps involving the generation of various organic intermediates. We estimate this heat of reaction by assuming PVDF breaks down completely to HF and elemental carbon. ΔH_6 is small compared to the other reactions listed, so any error from this estimate should be minimal. Reaction 5.7 is HF reacting with the Li_2CO_3 surface layer on the lithium metal anode formed in reaction 5.5 giving off water and carbon dioxide. This is also a relatively small exothermic reaction, but it is necessary for the remaining HF to first react with Li_2CO_3 before it can reach Li for reaction. Reaction 5.8 is the reaction of HF gas with the remaining Li in the anode. This is the most exothermic reaction in region IV, and we expect most of the heat at >400°C to come from this reaction.

Individual components and combinations of individual components heat flow results and discussion

Before testing microcells, we collected DSC heat flow data on individual components and combinations of components to better understand their behaviors and interactions. The resulting heat flow curves of these combinations of individual components are shown in **Figure 5.2**. **Table 5.2** provides the enthalpies found in these peaks and regions. In summary, there are 5 major interactions between the individual components shown in **Figure 5.2**: 1) Li uptake by LLZTO without

generating any significant heat, 2) PVDF pyrolysis to form HF, 3) $Li_{0.43}CoO_2$ phase transition and decomposition, 4) oxygen reaction with carbon to form CO_2, and, 5) HF reaction with lithium to form LiF and LiH. As described below, for these reactions our measured enthalpies are in good agreement with those expected from thermodynamic reference data.

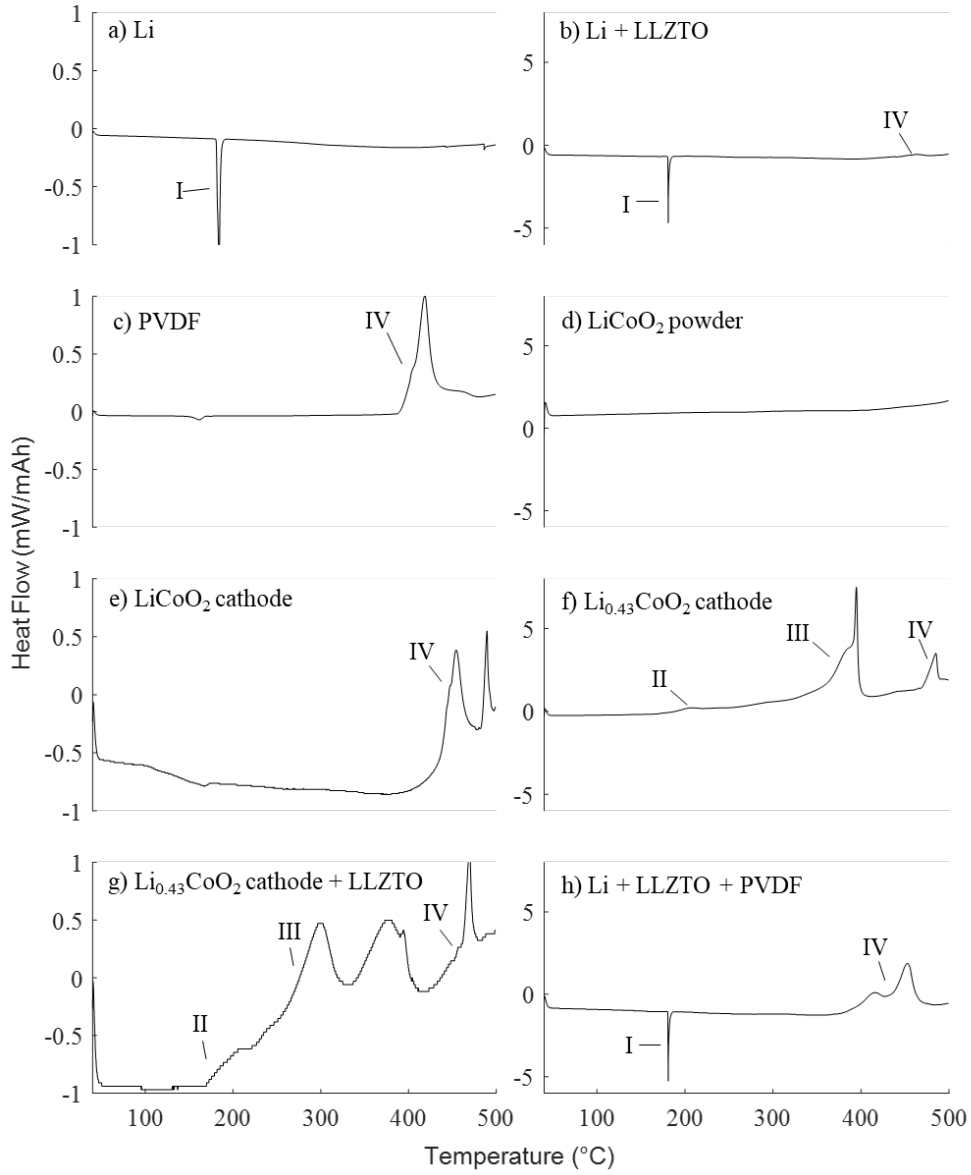

Figure 5.2. DSC heat flow for individual and combinations of individual components present in a cell-stack. This data has not been corrected to account for baseline drift. a) Li b) Li+LLZTO c) PVDF d) $LiCoO_2$ powder e) $LiCoO_2$ 0% SOC cathode sheet f) $Li_{0.43}CoO_2$ cathode sheet g) $Li_{0.43}CoO_2$ cathode sheet with LLZTO electrolyte h) Li+LLZTO+PVDF

In panel a), Li demonstrates thermal stability with the stainless-steel DSC pan; there is no noticeable heat flow apart from the lithium melting enthalpy in peak I, and the enthalpy of the melting peak remains unchanged in a second run, indicating that no lithium was consumed in the first run. In panel b), slight exothermic heat flow can be seen above 350°C which we attribute to molten lithium metal up-take by electron-rich LLZTO color centers potentially resulting in LLZTO fracture.[16,25] The amount of lithium consumed per mg of LLZTO we found to be within the range of 1.2 to 2.9 μg of Li per mg of LLZTO across three sample repeats. This value likely changes depending on the surface area to mass ratio of the LLZTO as well as the surface contact between the LLZTO and lithium. Different shapes of LLZTO shards could cause a change in the amount of Li uptake observed. The heat flow in panel b) indicates a small exothermic heat generation of -7.7×10^{-2} J/mAh or ~-5.9 J/g_{LLZTO}. In future calculations, we treat this heat flow as negligible, but the lithium consumption can be between 7 and 26% of the lithium sample in our microcells. In panel c), PVDF shows an endothermic melting point at ~170°C and an exothermic heat release in region IV which is consistent with the literature.[47,72,73] These peaks correspond to 9.4×10^{-3} J/mAh and -0.65 J/mAh respectively. The size of the endothermic melting enthalpy should change with the crystallinity of the PVDF polymer sample. Note that we do not include the melting peak of PVDF in **Table 5.3** as this peak is extremely small and should have little to no influence in cell self-heating. The enthalpy of complete pyrolysis of PVDF should remain constant regardless of the initial crystallinity. However, there may be some variation in the measured enthalpy as well as the onset temperature of pyrolysis depending on the pathway, polymer phase, and

extent of decomposition the fluoropolymer goes through.[74–76] We calculate the enthalpy of complete pyrolysis of PVDF at 25°C from the heat of formation to be -0.97 J/mAh, and we assume that PVDF decomposes entirely to carbon and HF; the measured enthalpy of PVDF pyrolysis should be lower than our calculated value. Panel d) shows no significant heat flow which indicates that $LiCoO_2$ powder is thermally stable by itself. In panel e), the $LiCoO_2$ cathode sheet shows heat release at about 400°C with an enthalpy of -0.72 mAh which should be due to PVDF breakdown as $LiCoO_2$, aluminum, and Super P should not generate any heat in this sample. This compares to the value of -0.65 J/mAh for the same breakdown reaction from panel c). A slight endotherm at ~170°C can be seen which is attributed to the PVDF melting point. In panel f), the $Li_{0.43}CoO_2$ cathode sheet shows heat release in region II due to the beginning of the phase transition of $Li_{0.43}CoO_2$ during decomposition which begins at ~170°C (below the melting point of lithium). The enthalpy of the peak in region III is ~-4.4 J/mAh which compares to the calculated value of -4.9 J/mAh for CO_2 formation. In a $Li_{0.43}CoO_2$ cathode sheet with 5 wt% Super P, carbon is stoichiometrically in excess for CO_2 formation assuming all the carbon is available to react with O_2. It is difficult to determine exactly how much of the total Super P present in the cathode sheet will spontaneously react with oxygen at 300°C due to significant variation in the reactivity of different forms of carbon which could lead to some variation in the heat flow in region III. [77] However, we think carbon active sites are still in excess as the integrated enthalpy in panel f) is within 5% of the thermodynamically calculated heat of formation of CO_2. The enthalpy of the peak in region IV of panel f) is -0.70 J/mAh which is comparable to the integrated

value of -0.65 J/mAh for PVDF pyrolysis measured in panel c). The heat release in region II appears as a slight double peak. We attribute this to an overlapping exothermic peak for the formation of an $LiCo_2O_4$ intermediate with small amounts of oxygen release and the subsequent endothermic decomposition of $LiCo_2O_4$ to release more oxygen. This peak has an integrated enthalpy of -0.66 J/mAh which compares to the calculated value of -0.54 J/mAh for the two-stage decomposition shown in Equations 2.1 and 2.2. The measured value is slightly larger than the calculated likely because the reaction between oxygen given off during decomposition and carbon as well as the reaction between oxygen and lithium are spontaneous at 230°C resulting in overlapping peaks. Other lithiation states may not go through the same decomposition pathway which could delay oxygen evolution and have a smaller reaction enthalpy for lower states of charge.[63,64,78] In panel g), the $Li_{0.43}CoO_2$ cathode sheet and LLZTO electrolyte show some level of reactivity. The cathode breaks down to form oxygen and CO_2 as it does in the absence of LLZTO at around ~200-250°C, and PVDF breaks down to form HF at ~400°C, but there is a third peak between 300°C and 400°C that is not seen in the cathode sheet or PVDF data. We think that this peak could be partially due to a direct surface reaction with CO_2 and LLZTO which occurs in dry carbon dioxide at room temperature.[79–81] In panel h), Li+LLZTO+PVDF sample shows a heat release of -2.8 J/mAh compared to calculated -5.03 J/mAh for Equation (5.8) at 400°C. We had an expected lithium consumption of 52% from Equation (5.8), and we observed lithium consumption of 58%. The discrepancy in lithium consumption can be attributed to the uptake of Li into LLZTO color centers which occurs at ~350°C with little to no heat generation.

Table 5.2. A summary of the integrated enthalpies for each combination of individual materials shown in **Figure 5.2**. All values shown are in J/mAh for a 160 mAh/g ($Li_{0.43}CoO_2$) LCO cathode sheet consisting of 90 wt% active material, 5 wt% PVDF, and 5 wt% Super P. A dash is present in boxes where no reaction is seen in that region.

	Peak I		Region II		Region III		Region IV		Post-Test Li Melting Enthalpy
	Measured	Calculated	Measured	Calculated	Measured	Calculated	Measured	Calculated	Measured
Li	0.11	0.11	--	--	--	--	--	--	0.11
Li + LLZTO	0.11	0.11	--	--	--	--	-7.7×10^{-2}	--	0.10
PVDF	--	--	--	--	--	--	-0.65	-0.97	--
$LiCoO_2$ powder	--	--	--	--	--	--	--	--	--
$LiCoO_2$ cathode	--	--	--	--	--	--	-0.72		--
$Li_{0.43}CoO_2$ cathode	--	--	-0.66		-4.4		-0.70		--
$Li_{0.43}CoO_2$ cathode + LLZTO	--	--	-0.66		--	--	--	--	--
Li + LLZTO + PVDF	0.12	0.11	--	--	--	--	-3.05		0.07

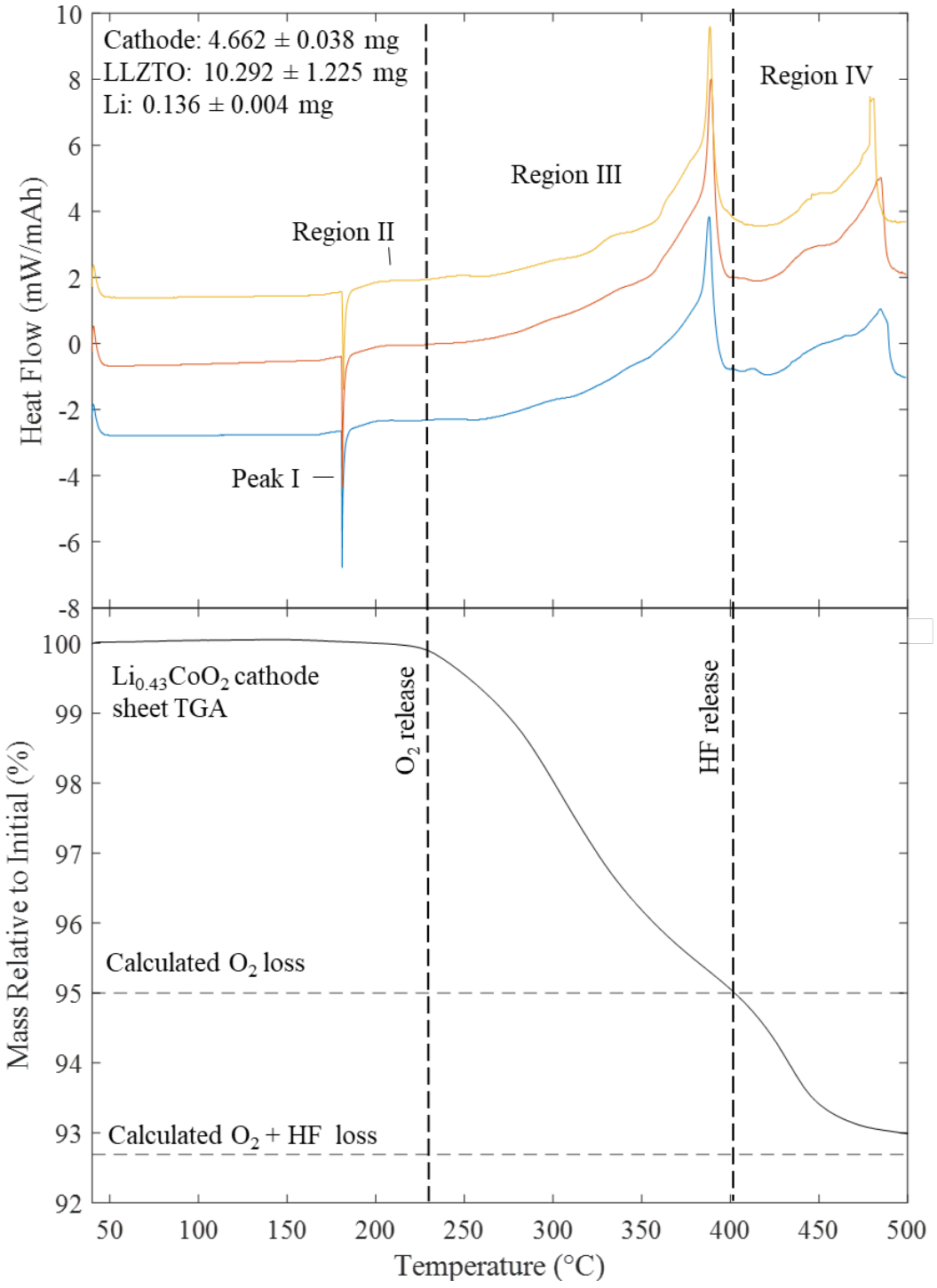

Figure 5.3. a) DSC heat flow of three replicates of a $Li_{0.43}CoO_2$ microcell with capacity matched electrodes taken at 2°C/min in a closed pan (top) with thermogravimetric analysis (TGA) of the

individual $Li_{0.43}CoO_2$ cathode sheet taken at 2°C/min in an open pan (bottom). The DSC data is offset by ±2 mW/mAh for visual clarify. (b) TGA result on a $Li_{0.43}CoO_2$ cathode sheet. Oxygen release begins at ~235°C according to Reactions 1 and 2, and HF release from PVDF breakdown (reaction 6) begins at ~400°C. Note that positive heat flow is exothermic in this figure.

Table 5.3. Summary of integrated results for each peak in each of the three microcell replicates shown in **Figure 5.3**. Note that negative enthalpies are exothermic

	Peak I	Region II	Region III	Region IV	Post-Test Li Melting Enthalpy
Microcell 1	0.12	-0.65	-7.39	-4.15	0
Microcell 2	0.12	-0.66	-9.16	-6.43	0
Microcell 3	0.11	-0.79	-7.74	-5.03	0

In **Figure 5.3**, we show the heat flow data for three $Li_{0.43}CoO_2$ microcell replicates assembled with nearly capacity matched electrodes along with the mass loss for a $Li_{0.43}CoO_2$ cathode sheet by itself. There are four different distinct heat flow peaks and regions: peak I with an integrated value of 0.12 J/mAh, region II with an integrated value of -0.65 J/mAh, region III with an integrated value of -7.39 J/mAh, and region IV with an integrated enthalpy of -4.15 J/mAh. These results are summarized for multiple microcell replicates in **Table 5.3.** Our cathode sheet shows mass loss starting at ~230°C which is in good agreement with stoichiometrically predicted mass loss from O_2 evolution during $Li_{0.43}CoO_2$ decomposition. We see a second region of mass loss starting at ~400°C which aligns with the stoichiometrically predicted mass loss due to HF evolution from PVDF pyrolysis. Therefore, all the reactions in region III should be driven primarily by oxygen, and most of the reactions in region IV should be driven by HF. We hypothesize a possible reaction system for thermal runaway of an LCO| LLZTO| Li battery shown in

Equations 5.1-5.8. The predicted enthalpies for of these reactions adjusted for elevated temperature are shown in **Figure 5.4**. We calculate all the reactions listed to be thermodynamically spontaneous between 200°C and 500°C.

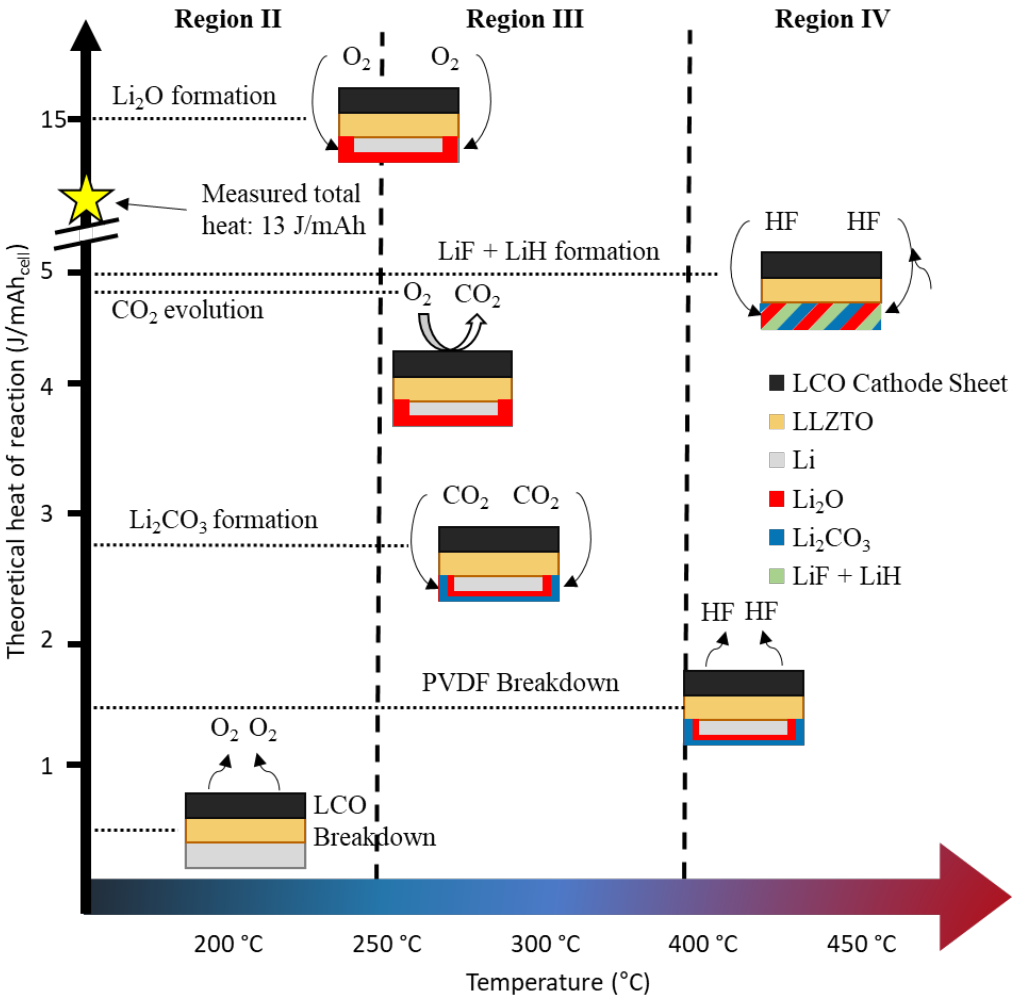

Figure 5.4. Map of the theoretical heats of reaction of thermochemical reactions within our microcell. All theoretical heats of reaction assume that lithium or the lithium containing reactant are in excess and have been adjusted for temperature.

Enthalpy Analysis and Reaction Thermochemistry

In **Figure 5.4** we present a map of the theoretical temperature-adjusted enthalpies for Equations 5.1-5.8. We used the reactions and enthalpies in **Figure 5.4.**, along with our measured values from **Figures 5.2** and **5.3**, to determine a reaction path or pathway. If 26% of the oxygen from $Li_{0.43}CoO_2$ decomposition (reactions 5.1 and 5.2) goes to Li_2O formation (reaction 5.3), the remaining 74% of oxygen goes to CO_2 evolution (reaction 5.4), and all other reactions go to completion, the calculated heat for region II is -0.65 J/mAh compared to the measured -0.65 J/mAh, the calculated heat for region III is -7.64 J/mAh compared to the measured --7.39 J/mAh for Microcell 1, and the calculated heat for region IV is -4.60 J/mAh compared to the measured --4.15 J/mAh for Microcell 1. **Figure 5.5** presents a visualization of the reaction path most consistent with our experimental results in the form of Sankey diagrams showing the mass balance and heat release.

Exothermic heat flow from reaction (2.1) starts at ~170°C, but oxygen release begins at ~230°C which is consistent with the literature.[78,82] Based off of first principles calculations previously reported in the literature, we initially assumed that any LCO cathode with a lithiation state less than 0.5 would go through equations 5.1 and 5.2 as a 2-stage decomposition. However, the delay in mass loss after the initial exotherm onset seems to suggest a multi-stage decomposition where no oxygen is released initially.[63] Given the decomposition of Li_xCoO_2 is inhomogeneous, the decomposition may vary locally and eventually follow equations 5.1 and 5.2 as the decomposition progresses.[64,83] We predict that initial oxygen released during LCO decomposition

reacts on the surface of molten lithium as well as with lithium vapor in a pool-fire method per Equation (5.3) to form an Li_2O crust-like surface layer via equation (5.3) which slows, but does not completely stop further reaction. Li_2O forms a semi-porous surface layer on lithium which is quantified with a Pillings-Bedworth ratio less of than 1 which indicates that the metal oxide molar volume is less than the metal molar volume resulting in a porous metal oxide.[39,84–87] The combined estimated heat for these two reactions is -0.54 J/mAh compared to the measured value of -0.65 J/mAh. During LCO decomposition, the lithium melting point of 180°C is reached and peak I occurs with a measured enthalpy of 0.11 J/mAh which compares to the literature lithium melting enthalpy of 0.11 J/mAh. Due to transport limitations impeding further reaction with lithium from the initial slowly growing Li_2O crust, oxygen reacts with Super P in the cathode shown in Equation (5.4), and most of the heat release in region III comes from CO_2 formation.[15,20] The evolved CO_2 then participates in a surface reaction with the Li_2O crust to form Li_2CO_3 by Equation (5.5) which acts as a more dense and stable surface layer than Li_2O.[71,85] The total enthalpy for peak III is --7.39 J/mAh which is 50.5% more than the expected heat from only CO_2 formation but 34.3% less than the expected for Li_2O formation indicating that both Li_2O and CO_2 formation are occurring simultaneously. In a 1:1 N:P ratio, lithium is the limiting reactant for Li_2O formation in an $Li_{0.43}CoO_2$ LiSSB. If lithium and oxygen were in stoichiometric balance for Li_2O formation (N:P ratio of 1.29), the expected heat from Li_2O would be -14.71 J/mAh. In a 1:1 N:P ratio, this expected heat release decreases to -11.51 J/mAh. Lithium carbonate and lithium oxide remain as a surface layer on lithium until PVDF decomposes to form HF by Equation (5.6) at ~400°C, and the HF

reacts with lithium carbonate per Equation (5.7). At this point, the HF and remaining lithium react to form LiF and LiH through Equation (5.8). Region IV integrates to an enthalpy of -4.15 J/mAh compared to the calculated value of -4.60 J/mAh from a summation of calculated heat from PVDF pyrolysis, Equation (5.7), and Equation (5.8). We estimate the expected heat from PVDF pyrolysis and subsequent HF reaction by assuming that PVDF decomposes entirely to carbon and HF. The decomposition of PVDF is a much more complicated, potentially multi-step, process that forms carbon chain intermediates.[74,75] It is also likely that not all of the fluorine is liberated from the polymer chain by 500°C.[88] In our predicted reaction pathway, after these reactions, there should no longer be any lithium or oxygen in the cell; but HF, water, argon, and carbon dioxide should remain in the gaseous state. We are unsure if and what these products react with in the cell after this reaction sequence. Upon holding the microcell at 500°C for 45 minutes after testing, we do not observe any further heat flow peaks. We plan to perform post-mortem chemical characterization on the microcells and *in-situ* gas analysis in future work to answer this question. LLZTO uptake of lithium shows no significant heat release despite consuming nearly 25% of the available lithium. LLZTO consumes a significant portion of the lithium anode at 350°C prior to HF evolution reducing the amount of lithium that participates in highly exothermic reactions.[25] In a commercial cell where the mass ratio between LLZTO and lithium will be smaller than what we use in our microcells, the potential heat release could be higher per mAh than what we see. LLZTO is one of the most stable solid ceramics against lithium; other oxide ceramics and sulfide ceramics such as LAGP, LATP, LGPS, and LPS would also react with the lithium anode resulting

in potentially more heat release compared to LLZTO with measured rates of temperature rise reaching >10,000 °C/min.[60,89] Even though we estimate that Super P reacts with 74% of the oxygen in system, the CO_2 formed continues to generate heat by reacting on the surface with the Li_2O crust on the lithium anode. Li_2CO_3 breakdown by HF consumes twice the number of moles of HF per mole of Li but produces 12% of the heat (464.28 kJ/mol HF vs. 56 kJ/mol HF). HF likely will react with the stable Li_2CO_3 and Li_2O crust initially which will expose pristine lithium to reaction with HF.

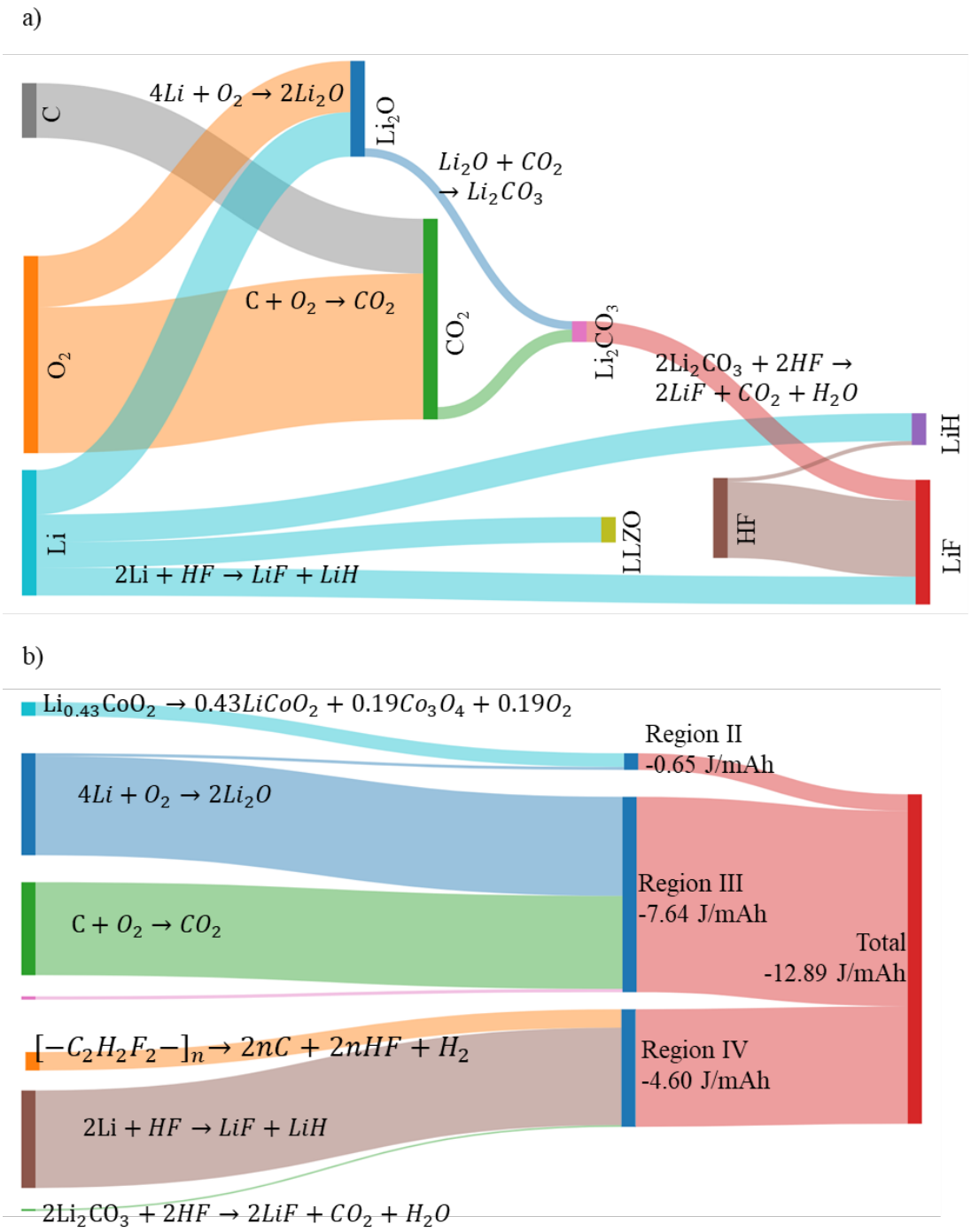

Figure 5.5. Sankey diagram showing a) the mass balance of lithium, carbon, and oxygen during our DSC testing and b) heat flow generated with each reaction. Note that the bar heights are proportional to the mass of each species in panel a) and the heat of each reaction in panel b).

Conclusions

Because the active materials themselves store and release energy in a battery, replacing the combustible organic electrolyte with a solid electrolyte does not automatically make a battery "safer", especially considering the push for lithium metal anodes. Ceramics like LLZTO can increase the onset temperature of self-heating (170-190°C for an LCO| LLZTO| Li cell compared to 80-100°C for modern Li-ion). We do not know when thermal runaway in a large-format cell will actually occur as our DSC heat flow data does not necessarily directly translate to heating rates (which have been traditionally used to define thermal runaway), but oxygen release occurs at ~230°C for LCO which is a required reactant for the highly exothermic Li_2O formation. This temperature of oxygen release will change for different cathode materials potentially resulting in lower onset temperatures of thermal runaway in cells made with high energy density cathode materials with lower thermal stability. This could make thermal management for thermal runaway prevention easier as higher temperatures (<170°C for LCO) may not lead to catastrophic thermal failure. However, other sources of heat generation capable of causing thermal runaway are still present such as oxygen evolution reacting to form Li_2O and CO_2, as well as fluorinated binder breakdown evolving HF at ~400°C. Molten lithium and oxygen do not react to completion when Super P is present in the cathode due to transport limitations imposed by an initial Li_2O layer which allows the carbon in the cathode to scavenge oxygen. The CO_2 produced participates in a surface reaction with the Li_2O crust on the lithium anode to form Li_2CO_3 which acts as a

more stable protective layer than Li_2O encouraging further oxygen scavenging by carbon. Additionally, the LLZTO consumes a significant portion of the lithium anode through lithium uptake with very little heat generation. Oxygen evolution from cathode decomposition is the principal driver of thermal runaway at temperatures <400°C for an LCO| LLZTO| Li battery. If oxygen is vented from the cell before it can react with lithium, carbon, or PVDF, then there is no other reaction between the cell components that can generate enough heat to cause thermal runaway prior to 400°C. The heat generation effects of fluorinated binder in particular can be problematic for lithium metal safety as highly reactive HF gas is the main driver of heat generation in region IV. This can significantly worsen thermal safety as HF reactions account for ~35% of the total heat generated in our DSC data. If the cell temperature reaches 400°C, self-heating can still occur due to binder breakdown generating HF, albeit to a lesser extent than if oxygen had not been vented.

Bibliography

(1) Goodenough, J. B.; Park, K. S. The Li-Ion Rechargeable Battery: A Perspective. *Journal of the American Chemical Society*. American Chemical Society January 30, 2013, pp 1167–1176. https://doi.org/10.1021/ja3091438.

(2) Wang, R.; Cui, W.; Chu, F.; Wu, F. Lithium Metal Anodes: Present and Future. *J. Energy Chem.* **2020**, *48*, 145–159. https://doi.org/10.1016/J.JECHEM.2019.12.024.

(3) Lin, D.; Liu, Y.; Cui, Y. Reviving the Lithium Metal Anode for High-Energy Batteries. *Nat. Nanotechnol. 2017 123* **2017**, *12* (3), 194–206. https://doi.org/10.1038/nnano.2017.16.

(4) Zhai, P.; Liu, L.; Gu, X.; Wang, T.; Gong, Y. Interface Engineering for Lithium Metal Anodes in Liquid Electrolyte. *Adv. Energy Mater.* **2020**, *10* (34), 2001257. https://doi.org/10.1002/AENM.202001257.

(5) Albertus, P.; Babinec, S.; Litzelman, S.; Newman, A. Status and Challenges in Enabling the Lithium Metal Electrode for High-Energy and Low-Cost Rechargeable Batteries. *Nat. Energy* **2018**, *3* (1), 16–21. https://doi.org/10.1038/s41560-017-0047-2.

(6) Cheng, X. B.; Zhang, R.; Zhao, C. Z.; Zhang, Q. Toward Safe Lithium Metal Anode in Rechargeable Batteries: A Review. *Chem. Rev.* **2017**, *117* (15), 10403–10473. https://doi.org/10.1021/ACS.CHEMREV.7B00115/ASSET/IMAGES/LARGE/CR-2017-00115D_0042.JPEG.

(7) Tarascon, J. M.; Armand, M. Issues and Challenges Facing Rechargeable Lithium Batteries. *Nat. 2001 4146861* **2001**, *414* (6861), 359–367. https://doi.org/10.1038/35104644.

(8) Xu, L.; Tang, S.; Cheng, Y.; Wang, K.; Liang, J.; Liu, C.; Cao, Y. C.; Wei, F.; Mai, L. Interfaces in Solid-State Lithium Batteries. *Joule* **2018**, *2* (10), 1991–2015. https://doi.org/10.1016/J.JOULE.2018.07.009.

(9) Manthiram, A.; Yu, X.; Wang, S. Lithium Battery Chemistries Enabled by Solid-State Electrolytes. *Nat. Rev. Mater. 2017 24* **2017**, *2* (4), 1–16. https://doi.org/10.1038/natrevmats.2016.103.

(10) Spotnitz, R.; Franklin, J. Abuse Behavior of High-Power, Lithium-Ion Cells. *J. Power Sources* **2003**, *113* (1), 81–100. https://doi.org/10.1016/S0378-7753(02)00488-3.

(11) Feng, X.; Ouyang, M.; Liu, X.; Lu, L.; Xia, Y.; He, X. Thermal Runaway Mechanism of Lithium Ion Battery for Electric Vehicles: A Review. *Energy Storage Materials*. Elsevier B.V. January 1, 2018, pp 246–267. https://doi.org/10.1016/j.ensm.2017.05.013.

(12) Zheng, F.; Kotobuki, M.; Song, S.; Lai, M. O.; Lu, L. Review on Solid Electrolytes for All-Solid-State Lithium-Ion Batteries. *J. Power Sources* **2018**, *389*, 198–213. https://doi.org/10.1016/j.jpowsour.2018.04.022.

(13) Johnson, N. B.; Albertus, P. Modeling Thermal Behavior and Safety of Large Format All-Solid-State Lithium Metal Batteries under Thermal Ramp and Short Circuit Conditions. *J. Electrochem. Soc.* **2022**, *169* (6), 060546. https://doi.org/10.1149/1945-7111/ac79cf.

(14) Bates, A. M.; Preger, Y.; Torres-Castro, L.; Harrison, K. L.; Harris, S. J.; Hewson, J. Are Solid-State Batteries Safer than Lithium-Ion Batteries? *Joule* **2022**, *6* (4), 742–755. https://doi.org/10.1016/j.joule.2022.02.007.
(15) Inoue, T.; Mukai, K. Are All-Solid-State Lithium-Ion Batteries Really Safe?−verification by Differential Scanning Calorimetry with an All-Inclusive Microcell. *ACS Appl. Mater. Interfaces* **2017**, *9* (2), 1507–1515. https://doi.org/10.1021/acsami.6b13224.
(16) Chen, R.; Nolan, A. M.; Lu, J.; Wang, J.; Yu, X.; Mo, Y.; Chen, L.; Huang, X.; Li, H. The Thermal Stability of Lithium Solid Electrolytes with Metallic Lithium. *Joule* **2020**, *4* (4), 812–821. https://doi.org/10.1016/j.joule.2020.03.012.
(17) Janek, J.; Zeier, W. G. A Solid Future for Battery Development. *Nat. Energy* **2016**, *1* (9). https://doi.org/10.1038/nenergy.2016.141.
(18) MacNeil, D. D.; Dahn, J. R. The Reactions of $Li_{0.5}CoO_2$ with Nonaqueous Solvents at Elevated Temperatures. *J. Electrochem. Soc.* **2002**, *149* (7), A912. https://doi.org/10.1149/1.1483865.
(19) Macneil, D. D.; Christensen, L.; Landucci, J.; Paulsen, J. M.; Dahn, J. R. An Autocatalytic Mechanism for the Reaction of Li_xCoO_2 in Electrolyte at Elevated Temperature. *J. Electrochem. Soc.* **2000**, *147* (3), 970–979.
(20) Yamaki, J.; Shinjo, Y.; Doi, T.; Okada, S. The Rate Equation for Oxygen Evolution by Decomposition of Li_xCoO_2 at Elevated Temperatures. *J. Electrochem. Soc.* **2014**, *161* (10), A1648–A1654. https://doi.org/10.1149/2.0621410jes.
(21) Jeppson, D. W.; Ballif, J. L.; Yuan, W. W.; Chou, B. E. *Lithium Literature Review: Lithium's Properties and Interactions*; N.P.: United States, 1978. https://doi.org/10.2172/6885395.
(22) Feng, X.; Fang, M.; He, X.; Ouyang, M.; Lu, L.; Wang, H.; Zhang, M. Thermal Runaway Features of Large Format Prismatic Lithium Ion Battery Using Extended Volume Accelerating Rate Calorimetry. *J. Power Sources* **2014**, *255*, 294–301. https://doi.org/10.1016/j.jpowsour.2014.01.005.
(23) Chen, S. C.; Wan, C. C.; Wang, Y. Y. Thermal Analysis of Lithium-Ion Batteries. *J. Power Sources* **2005**, *140* (1), 111–124. https://doi.org/10.1016/j.jpowsour.2004.05.064.
(24) Steinhardt, M.; Gillich, E. I.; Rheinfeld, A.; Kraft, L.; Spielbauer, M.; Bohlen, O.; Jossen, A. Low-Effort Determination of Heat Capacity and Thermal Conductivity for Cylindrical 18650 and 21700 Lithium-Ion Cells. *J. Energy Storage* **2021**, *42*, 103065. https://doi.org/10.1016/j.est.2021.103065.
(25) Wolfenstine, J.; Allen, J. L.; Read, J.; Sakamoto, J. Chemical Stability of Cubic $Li_7La_3Zr_2O_{12}$ with Molten Lithium at Elevated Temperature. *J. Mater. Sci.* **2013**, *48* (17), 5846–5851. https://doi.org/10.1007/S10853-013-7380-Z/FIGURES/5.
(26) Lamb, J.; Torres-Castro, L. United States Advanced Battery Consortium BatteryAbuse Testing Manual for Electric and Hybrid Vehicle Applications. US DOE Vehicle Technology Program 2022.
(27) MacNeil, D. D.; Dahn, J. R. The Reaction of Charged Cathodes with

Nonaqueous Solvents and Electrolytes: I. $Li_{0.5}CoO_2$. *J. Electrochem. Soc.* **2001**, *148* (11), A1205. https://doi.org/10.1149/1.1407245.
(28) Ren, D.; Liu, X.; Feng, X.; Lu, L.; Ouyang, M.; Li, J.; He, X. Model-Based Thermal Runaway Prediction of Lithium-Ion Batteries from Kinetics Analysis of Cell Components. *Appl. Energy* **2018**, *228*, 633–644. https://doi.org/10.1016/j.apenergy.2018.06.126.
(29) Hatchard, T. D.; MacNeil, D. D.; Basu, A.; Dahn, J. R. Thermal Model of Cylindrical and Prismatic Lithium-Ion Cells. *J. Electrochem. Soc.* **2002**, *148* (7), A755–A761. https://doi.org/10.1149/1.1377592.
(30) Kim, G. H.; Pesaran, A.; Spotnitz, R. A Three-Dimensional Thermal Abuse Model for Lithium-Ion Cells. *J. Power Sources* **2007**, *170* (2), 476–489. https://doi.org/10.1016/j.jpowsour.2007.04.018.
(31) Liu, X.; Wu, Z.; Stoliarov, S. I.; Denlinger, M.; Masias, A.; Snyder, K. A Thermo-Kinetic Model of Thermally-Induced Failure of a Lithium Ion Battery: Development, Validation and Application. *J. Electrochem. Soc.* **2018**, *165* (11), A2909–A2918. https://doi.org/10.1149/2.0111813jes.
(32) MacNeil, D. D.; Dahn, J. R. Test of Reaction Kinetics Using Both Differential Scanning and Accelerating Rate Calorimetries As Applied to the Reaction of Li_xCoO_2 in Non-Aqueous Electrolyte. *J. Phys. Chem. A* **2002**, *105* (18), 4430–4439. https://doi.org/10.1021/jp001187j.
(33) Ostanek, J. K.; Li, W.; Mukherjee, P. P.; Crompton, K. R.; Hacker, C. Simulating Onset and Evolution of Thermal Runaway in Li-Ion Cells Using a Coupled Thermal and Venting Model. *Appl. Energy* **2020**, *268*, 114972. https://doi.org/10.1016/j.apenergy.2020.114972.
(34) Spotnitz, R. M.; Weaver, J.; Yeduvaka, G.; Doughty, D. H.; Roth, E. P. Simulation of Abuse Tolerance of Lithium-Ion Battery Packs. *J. Power Sources* **2007**, *163* (2), 1080–1086. https://doi.org/10.1016/j.jpowsour.2006.10.013.
(35) L. Gao; S.Liu; Dougal, R. A. Dynamic Lithium-Ion Battery Model for System Simulation. *IEEE Trans. Compon. Packag. Technol.* **2002**, *25* (3), 495–505. https://doi.org/10.1109/TCAPT.2002.803653.
(36) Lopez, C. F.; Jeevarajan, J. A.; Mukherjee, P. P. Experimental Analysis of Thermal Runaway and Propagation in Lithium-Ion Battery Modules. *J. Electrochem. Soc.* **2015**, *162* (9), A1905–A1915. https://doi.org/10.1149/2.0921509jes.
(37) Fuller, T. F.; Harb, J. N. *Electrochemical Engineering*; 2018; Vol. 1.
(38) Furushima, Y.; Yanagisawa, C.; Nakagawa, T.; Aoki, Y.; Muraki, N. Thermal Stability and Kinetics of Delithiated $LiCoO_2$. *J. Power Sources* **2011**, *196* (4), 2260–2263. https://doi.org/10.1016/j.jpowsour.2010.09.076.
(39) Schiemann, M.; Bergthorson, J.; Fischer, P.; Scherer, V.; Taroata, D.; Schmid, G. A Review on Lithium Combustion. *Applied Energy*. Elsevier January 15, 2016, pp 948–965. https://doi.org/10.1016/j.apenergy.2015.10.172.
(40) Liu, B.; Yin, S.; Xu, J. Integrated Computation Model of Lithium-Ion Battery Subject to Nail Penetration. *Appl. Energy* **2016**, *183*, 278–289. https://doi.org/10.1016/j.apenergy.2016.08.101.

(41) Zhao, R.; Liu, J.; Gu, J. Simulation and Experimental Study on Lithium Ion Battery Short Circuit. *Appl. Energy* **2016**, *173*, 29–39. https://doi.org/10.1016/j.apenergy.2016.04.016.
(42) Kupper, C.; Spitznagel, S.; Döring, H.; Danzer, M. A.; Gutierrez, C.; Kvasha, A.; Bessler, W. G. Combined Modeling and Experimental Study of the High-Temperature Behavior of a Lithium-Ion Cell: Differential Scanning Calorimetry, Accelerating Rate Calorimetry and External Short Circuit. *Electrochim. Acta* **2019**, *306*, 209–219. https://doi.org/10.1016/j.electacta.2019.03.079.
(43) Sturm, J.; Rheinfeld, A.; Buzon, D.; Jossen, A. On The Impact of the Locality on Short-Circuit Characteristics: Experimental Analysis and Multiphysics Simulation of External and Local Short-Circuits Applied to Lithium-Ion Batteries. *J. Electrochem. Soc.* **2020**, *167* (9), 090521. https://doi.org/10.1149/1945-7111/ab8873.
(44) Liu, X.; Stoliarov, S. I.; Denlinger, M.; Masias, A.; Snyder, K. Comprehensive Calorimetry of the Thermally-Induced Failure of a Lithium Ion Battery. *J. Power Sources* **2015**, *280*, 516–525. https://doi.org/10.1016/j.jpowsour.2015.01.125.
(45) Liu, X.; Wu, Z.; Stoliarov, S. I.; Denlinger, M.; Masias, A.; Snyder, K. Heat Release during Thermally-Induced Failure of a Lithium Ion Battery: Impact of Cathode Composition. *Fire Saf. J.* **2016**, *85*, 10–22. https://doi.org/10.1016/j.firesaf.2016.08.001.
(46) Feng, X.; Ren, D.; He, X.; Ouyang, M. Mitigating Thermal Runaway of Lithium-Ion Batteries. *Joule*. Cell Press April 15, 2020, pp 743–770. https://doi.org/10.1016/j.joule.2020.02.010.
(47) Kriston, A.; Adanouj, I.; Ruiz, V.; Pfrang, A. Quantification and Simulation of Thermal Decomposition Reactions of Li-Ion Battery Materials by Simultaneous Thermal Analysis Coupled with Gas Analysis. *J. Power Sources* **2019**, *435*, 226774. https://doi.org/10.1016/j.jpowsour.2019.226774.
(48) Bock, R.; Onsrud, M.; Karoliussen, H.; Pollet, B. G.; Seland, F.; Burheim, O. S. Thermal Gradients with Sintered Solid State Electrolytes in Lithium-Ion Batteries. **2020**, *13* (1), 253.
(49) Takahata, K.; Terasaki, I. Thermal Conductivity of A_xBO_2-Type Layered Oxides $Na_{0.77}MnO_2$ and $LiCoO_2$. *Jpn. J. Appl. Phys., Part 1* **2002**, *41* (2 A), 763–764. https://doi.org/10.1143/jjap.41.763.
(50) Cho, J.; Losego, M. D.; Zhang, H. G.; Kim, H.; Zuo, J.; Petrov, I.; Cahill, D. G.; Braun, P. V. Electrochemically Tunable Thermal Conductivity of Lithium Cobalt Oxide. *Nat. Commun.* **2014**, *5* (1), 1–6. https://doi.org/10.1038/ncomms5035.
(51) *CRC Handbook of Chemistry and Physics*, 85th ed.; Lide, D. R., Ed.; CRC Press: Cleveland, Ohio, 1978.
(52) Cooke, J. W. Experimental Determination of the Thermal Conductivity of Molten Lithium from 320° to 830°C. *J. Chem. Phys.* **1964**, *40* (7), 1902–1909. https://doi.org/10.1063/1.1725421.
(53) Awaka, J.; Kijima, N.; Hayakawa, H.; Akimoto, J. Synthesis and Structure

Analysis of Tetragonal $Li_7La_3Zr_2O_{12}$ with the Garnet-Related Type Structure. *J. Solid State Chem.* **2009**, *182* (8), 2046–2052. https://doi.org/10.1016/j.jssc.2009.05.020.

(54) Zhang, X.; Oh, T.-S.; Fergus, J. W. Densification of Ta-Doped Garnet-Type $Li_{6.75}La_3Zr_{1.75}Ta_{0.25}O_{12}$ Solid Electrolyte Materials by Sintering in a Lithium-Rich Air Atmosphere. *J. Electrochem. Soc.* **2019**, *166* (15), A3753–A3759. https://doi.org/10.1149/2.1031915jes.

(55) Loges, A.; Herberger, S.; Seegert, P.; Wetzel, T. A Study on Specific Heat Capacities of Li-Ion Cell Components and Their Influence on Thermal Management. *J. Power Sources* **2016**, *336*, 341–350. https://doi.org/10.1016/j.jpowsour.2016.10.049.

(56) Gotcu-Freis, P.; Cupid, D. M.; Rohde, M.; Seifert, H. J. New Experimental Heat Capacity and Enthalpy of Formation of Lithium Cobalt Oxide. *J. Chem. Thermodyn.* **2015**, *84*, 118–127. https://doi.org/10.1016/j.jct.2014.12.007.

(57) Il'ina, E. A.; Raskovalov, A. A.; Reznitskikh, O. G. Thermodynamic Properties of Solid Electrolyte $Li_7La_3Zr_2O_{12}$. *J. Chem. Thermodyn.* **2019**, *128*, 68–73. https://doi.org/10.1016/j.jct.2018.08.009.

(58) Nelson, P.; Shabbir, A.; Gallagher, K.; Dees, D. *Modeling the Performance and Cost of Lithium-Ion Batteries for Electric-Drive Vehicles Chemical Sciences and Engineering Division*; Argonne, IL (United States), 2019. https://doi.org/10.2172/1503280.

(59) Bak, S. M.; Hu, E.; Zhou, Y.; Yu, X.; Senanayake, S. D.; Cho, S. J.; Kim, K. B.; Chung, K. Y.; Yang, X. Q.; Nam, K. W. Structural Changes and Thermal Stability of Charged $LiNi_xMn_yCo_zO_2$ Cathode Materials Studied by Combined in Situ Time-Resolved XRD and Mass Spectroscopy. *ACS Appl. Mater. Interfaces* **2014**, *6* (24), 22594–22601. https://doi.org/10.1021/am506712c.

(60) Vishnugopi, B. S.; Hasan, M. T.; Zhou, H.; Mukherjee, P. P. Interphases and Electrode Crosstalk Dictate the Thermal Stability of Solid-State Batteries. *ACS Energy Lett.* **2022**, *8*, 398–407. https://doi.org/10.1021/ACSENERGYLETT.2C02443.

(61) Belharouak, I.; Lu, W.; Vissers, D.; Amine, K. Safety Characteristics of Li(Ni0.8Co0.15Al0.05)O2 and Li(Ni1/3Co1/3Mn1/3)O2. *Electrochem. Commun.* **2006**, *8* (2), 329–335. https://doi.org/10.1016/J.ELECOM.2005.12.007.

(62) Kondo, H.; Baba, N.; Makimura, Y.; Itou, Y.; Kobayashi, T. Model Validation and Simulation Study on the Thermal Abuse Behavior of $LiNi_{0.8}Co_{0.15}Al_{0.05}O_2$-Based Batteries. *J. Power Sources* **2020**, *448*, 227464. https://doi.org/10.1016/j.jpowsour.2019.227464.

(63) Wang, L.; Maxisch, T.; Ceder, G. A First-Principles Approach to Studying the Thermal Stability of Oxide Cathode Materials. *Chem. Mater.* **2007**, *19* (3), 543–552. https://doi.org/10.1021/cm0620943.

(64) Shurtz, R. C. A Thermodynamic Reassessment of Lithium-Ion Battery Cathode Calorimetry. *J. Electrochem. Soc.* **2020**, *167* (14), 140544. https://doi.org/10.1149/1945-7111/abc7b4.

(65) Zhang, H.; May, B. M.; Omenya, F.; Whittingham, M. S.; Cabana, J.; Zhou, G.

Layered Oxide Cathodes for Li-Ion Batteries: Oxygen Loss and Vacancy Evolution. *Chem. Mater.* **2019**, *31* (18), 7790–7798. https://doi.org/10.1021/ACS.CHEMMATER.9B03245/ASSET/IMAGES/MEDIUM/CM9B03245_M001.GIF.

(66) Huang, Y.; Lin, Y. C.; Jenkins, D. M.; Chernova, N. A.; Chung, Y.; Radhakrishnan, B.; Chu, I. H.; Fang, J.; Wang, Q.; Omenya, F.; Ong, S. P.; Whittingham, M. S. Thermal Stability and Reactivity of Cathode Materials for Li-Ion Batteries. *ACS Appl. Mater. Interfaces* **2016**, *8* (11), 7013–7021. https://doi.org/10.1021/ACSAMI.5B12081/ASSET/IMAGES/AM-2015-12081W_M013.GIF.

(67) Hurt, R. H.; Haynes, B. S. On the Origin of Power-Law Kinetics in Carbon Oxidation. *Proc. Combust. Inst.* **2005**, *30* (2), 2161–2168. https://doi.org/10.1016/J.PROCI.2004.08.131.

(68) Swann, J. D.; Stoliarov, S. I. Determination of Pyrolysis and Combustion Properties of Poly(Vinylidene Fluoride) Using Comprehensive Modeling: Relating Heat Transfer to the Intumescent Char's Porous Structure. *Fire Saf. J.* **2021**, *120*, 103086. https://doi.org/10.1016/J.FIRESAF.2020.103086.

(69) Coman, P. T.; Rayman, S.; White, R. E. A Lumped Model of Venting during Thermal Runaway in a Cylindrical Lithium Cobalt Oxide Lithium-Ion Cell. *J. Power Sources* **2016**, *307*, 56–62. https://doi.org/10.1016/J.JPOWSOUR.2015.12.088.

(70) Markevich, E.; Salitra, G.; Aurbach, D. Influence of the PVdF Binder on the Stability of $LiCoO_2$ Electrodes. *Electrochem. Commun.* **2005**, *7* (12), 1298–1304. https://doi.org/10.1016/j.elecom.2005.09.010.

(71) Mosqueda, H. A.; Vazquez, C.; Bosch, P.; Pfeiffer, H. Chemical Sorption of Carbon Dioxide (CO2) on Lithium Oxide (Li2O). *Chem. Mater.* **2006**, *18* (9), 2307–2310. https://doi.org/10.1021/CM060122B/ASSET/IMAGES/LARGE/CM060122BF00009.JPEG.

(72) Gregorio, R.; Cestari, M. Effect of Crystallization Temperature on the Crystalline Phase Content and Morphology of Poly(Vinylidene Fluoride). *J. Polym. Sci. Part B Polym. Phys.* **1994**, *32* (5), 859–870. https://doi.org/10.1002/POLB.1994.090320509.

(73) Prest, W. M.; Luca, D. J. The Morphology and Thermal Response of High-temperature–Crystallized Poly(Vinylidene Fluoride). *J. Appl. Phys.* **2008**, *46* (10), 4136. https://doi.org/10.1063/1.321438.

(74) O'shea, M. L.; Morterra, C.; Low, M. J. D. Spectroscopic Studies of Carbons. XVII. Pyrolysis of Polyvinylidene Fluoride. *Mater. Chem. Phys.* **1990**, *26* (2), 193–209. https://doi.org/10.1016/0254-0584(90)90038-C.

(75) Xu, Z. X.; Zhang, C. X.; He, Z. X.; Wang, Q. Pyrolysis Characteristic and Kinetics of Polyvinylidene Fluoride with and without Pine Sawdust. *J. Anal. Appl. Pyrolysis* **2017**, *123*, 402–408. https://doi.org/10.1016/j.jaap.2016.10.027.

(76) Botelho, G.; Lanceros-Mendez, S.; Gonçalves, A. M.; Sencadas, V.; Rocha, J. G. Relationship between Processing Conditions, Defects and Thermal

Degradation of Poly(Vinylidene Fluoride) in the β-Phase. *J. Non. Cryst. Solids* **2008**, *354* (1), 72–78. https://doi.org/10.1016/j.jnoncrysol.2007.07.012.
(77) Donnet, J. B. Structure and Reactivity of Carbons: From Carbon Black to Carbon Composites. *Carbon N. Y.* **1982**, *20* (4), 267–282. https://doi.org/10.1016/0008-6223(82)90002-1.
(78) Baba, Y.; Okada, S.; Yamaki, J. ichi. Thermal Stability of Li_xCoO_2 Cathode for Lithium Ion Battery. *Solid State Ionics* **2002**, *148* (3–4), 311–316. https://doi.org/10.1016/S0167-2738(02)00067-X.
(79) Wang, Y.; Lai, W. Phase Transition in Lithium Garnet Oxide Ionic Conductors Li7La3Zr2O12: The Role of Ta Substitution and H2O/CO2 Exposure. *J. Power Sources* **2015**, *275*, 612–620. https://doi.org/10.1016/J.JPOWSOUR.2014.11.062.
(80) Kang, S. G.; Sholl, D. S. First-Principles Study of Chemical Stability of the Lithium Oxide Garnets Li7La3M2O12 (M = Zr, Sn, or Hf). *J. Phys. Chem. C* **2014**, *118* (31), 17402–17406. https://doi.org/10.1021/JP504314W/ASSET/IMAGES/LARGE/JP-2014-04314W_0004.JPEG.
(81) Cheng, L.; Wu, C. H.; Jarry, A.; Chen, W.; Ye, Y.; Zhu, J.; Kostecki, R.; Persson, K.; Guo, J.; Salmeron, M.; Chen, G.; Doeff, M. Interrelationships among Grain Size, Surface Composition, Air Stability, and Interfacial Resistance of Al-Substituted Li7La3Zr2O12 Solid Electrolytes. *ACS Appl. Mater. Interfaces* **2015**, *7* (32), 17649–17655. https://doi.org/10.1021/ACSAMI.5B02528/ASSET/IMAGES/AM-2015-02528Q_M004.GIF.
(82) Dahn, J. R.; Fuller, E. W.; Obrovac, M.; von Sacken, U. Thermal Stability of LixCoO2, LixNiO2 and λ-MnO2 and Consequences for the Safety of Li-Ion Cells. *Solid State Ionics* **1994**, *69* (3–4), 265–270. https://doi.org/10.1016/0167-2738(94)90415-4.
(83) Sharifi-Asl, S.; Soto, F. A.; Nie, A.; Yuan, Y.; Asayesh-Ardakani, H.; Foroozan, T.; Yurkiv, V.; Song, B.; Mashayek, F.; Klie, R. F.; Amine, K.; Lu, J.; Balbuena, P. B.; Shahbazian-Yassar, R. Facet-Dependent Thermal Instability in LiCoO2. *Nano Lett.* **2017**, *17* (4), 2165–2171. https://doi.org/10.1021/ACS.NANOLETT.6B04502/ASSET/IMAGES/LARGE/NL-2016-045025_0004.JPEG.
(84) Markowitz, M. M.; Boryta, D. A. Lithium Metal-Gas Reactions. Interaction of Lithium Metal with Air and Its Component Gases. *J. Chem. Eng. Data* **1962**, *7* (4), 586–591. https://doi.org/10.1021/JE60015A047/ASSET/JE60015A047.FP.PNG_V03.
(85) Otto, S. K.; Fuchs, T.; Moryson, Y.; Lerch, C.; Mogwitz, B.; Sann, J.; Janek, J.; Henss, A. Storage of Lithium Metal: The Role of the Native Passivation Layer for the Anode Interface Resistance in Solid State Batteries. *ACS Appl. Energy Mater.* **2021**, *4* (11), 12798–12807. https://doi.org/10.1021/ACSAEM.1C02481/ASSET/IMAGES/LARGE/AE1C02481_0007.JPEG.
(86) Sharafi, A.; Kazyak, E.; Davis, A. L.; Yu, S.; Thompson, T.; Siegel, D. J.;

Dasgupta, N. P.; Sakamoto, J. Surface Chemistry Mechanism of Ultra-Low Interfacial Resistance in the Solid-State Electrolyte Li7La3Zr2O12. *Chem. Mater.* **2017**, *29* (18), 7961–7968. https://doi.org/10.1021/ACS.CHEMMATER.7B03002/ASSET/IMAGES/LARGE/CM-2017-03002V_0005.JPEG.

(87) Kinzer, B.; Davis, A. L.; Krauskopf, T.; Hartmann, H.; LePage, W. S.; Kazyak, E.; Janek, J.; Dasgupta, N. P.; Sakamoto, J. Operando Analysis of the Molten Li|LLZO Interface: Understanding How the Physical Properties of Li Affect the Critical Current Density. *Matter* **2021**, *4* (6), 1947–1961. https://doi.org/10.1016/J.MATT.2021.04.016.

(88) Madorsky, S. I.; Hart, V. E.; Straus, S.; Sedlak, V. A. Thermal Degradation of Tetrafluoroethylene and Hydrofluoroethylene Polymers in a Vacuum. *J. Res. Natl. Bur. Stand. (1934).* **1953**, *51* (6), 327. https://doi.org/10.6028/jres.051.036.

(89) Wang, C.; Fu, K.; Kammampata, S. P.; McOwen, D. W.; Samson, A. J.; Zhang, L.; Hitz, G. T.; Nolan, A. M.; Wachsman, E. D.; Mo, Y.; Thangadurai, V.; Hu, L. Garnet-Type Solid-State Electrolytes: Materials, Interfaces, and Batteries. *Chem. Rev.* **2020**, *120* (10), 4257–4300. https://doi.org/10.1021/ACS.CHEMREV.9B00427/ASSET/IMAGES/ACS.CHEMREV.9B00427.SOCIAL.JPEG_V03.